

VAPORIZATION CHARACTERISTICS OF MONODISPERSED
MULTICOMPONENT FUEL DROPLETS IN AN OPPOSED
STAGNATION FLOW

by
Changshun Sun

ProQuest Number: 10795360

All rights reserved

INFORMATION TO ALL USERS

The quality of this reproduction is dependent upon the quality of the copy submitted.

In the unlikely event that the author did not send a complete manuscript and there are missing pages, these will be noted. Also, if material had to be removed, a note will indicate the deletion.



ProQuest 10795360

Published by ProQuest LLC (2018). Copyright of the Dissertation is held by the Author.

All rights reserved.

This work is protected against unauthorized copying under Title 17, United States Code
Microform Edition © ProQuest LLC.

ProQuest LLC.
789 East Eisenhower Parkway
P.O. Box 1346
Ann Arbor, MI 48106 – 1346

T 6889

C. 2

A thesis submitted to the Faculty and Board of Trustees of the Colorado School of Mines in partial fulfillment of the requirements for the degree of Master of Science (Engineering).

Golden, Colorado

Date: 08/31/2011

Signed: Changshun Sun
Changshun Sun

Approved: Robert J. Kee 8/31/11
Dr. Robert J. Kee
Thesis Advisor

Golden, Colorado

Date: 08/31/2011

G. Mustoe for K.L. Moore
Dr. Kevin L. Moore
Professor and Department Head
Mechanical Engineering

ABSTRACT

Internal combustion engines and gas turbines are typically designed to burn liquid fuels, which are often a blend of hydrocarbon and oxygenated compounds. Gas-phase combustion follows the vaporization of fuel sprays. The objective of this thesis is to assist understanding of vaporization characteristics of monodispersed multicomponent liquid fuel droplets. A computational model is developed and applied to study droplet vaporization in an opposed-flow stagnation flow field. Fuel droplets are entrained into one side of the opposed flow, with the opposing flow being air. Although the stagnation-flow configuration is idealized, the flow conditions are chosen to be relevant to practical combustion environments. The two-phase computation algorithm is based on an iterative coupling between an Eulerian finite-volume representation of the gas flow and a Lagrangian representation of the vaporizing droplet trajectories. In this study, the droplets may be mixtures of heptane, dodecane, tetradecane, diesel fuel, and ethanol. The model is used to study droplet vaporization characteristics as functions of numerous parameters, including droplet size, composition, and number density. The flow conditions are varied to study the effects of temperature, pressure, and velocity.

TABLE OF CONTENTS

ABSTRACT	iii
LIST OF FIGURES	vi
LIST OF TABLES	viii
ACKNOWLEDGMENTS	ix
CHAPTER 1 INTRODUCTION	1
CHAPTER 2 LITERATURE REVIEW	5
CHAPTER 3 MODEL DEVELOPMENT	13
3.1 Eulerian Gas-phase Conservation Equations	15
3.2 Lagrangian Droplets Dynamics	16
3.3 Droplet Vaporization	18
3.3.1 Droplet Heat Transfer	20
3.3.2 Droplet Momentum	21
3.3.3 Gas-phase Source Terms	22
3.4 Gas-phase Kinetics	23
3.5 Numerical Algorithm	23
3.6 Liquid Fuel Properties	26
CHAPTER 4 RESULTS AND DISCUSSION	29
4.1 Initial Equivalence Ratio and Droplet Loading	29
4.2 Ethanol-heptane Liquid Fuels	30
4.3 Heptane-dodecane-tetradecane Liquid Fuels	33
4.4 Dodecane-tetradecane-hexadecane Liquid Fuels	39

CHAPTER 5 SUMMARY AND CONCLUSIONS 43
REFERENCES CITED 47

LIST OF FIGURES

Figure 1.1	Opposed flow liquid fuel droplet vaporization configuration.	2
Figure 3.1	Illustration of evaporating droplet motion, crossing the Eulerian mesh boundaries.	22
Figure 3.2	Physical properties of liquid heptane, dodecane, tetradecane and diesel.	26
Figure 3.3	Physical properties of liquid heptane, methanol and ethanol.	28
Figure 4.1	Solution profiles for 5 μm droplets with a composition of 85% $\text{C}_2\text{H}_5\text{OH}$ and 15% C_7H_{16} carried in air, $U_{\text{in}} = 100 \text{ cm s}^{-1}$, $T_{\text{in}} = 47 \text{ }^\circ\text{C}$, and $p = 1 \text{ atm}$	31
Figure 4.2	Solution profiles for 10 μm droplets with a composition of 85% $\text{C}_2\text{H}_5\text{OH}$ and 15% C_7H_{16} carried in air, $U_{\text{in}} = 100 \text{ cm s}^{-1}$, $T_{\text{in}} = 47 \text{ }^\circ\text{C}$, and $p = 1 \text{ atm}$	32
Figure 4.3	Solution profiles for 40 μm droplets with a composition of 85% $\text{C}_2\text{H}_5\text{OH}$ and 15% C_7H_{16} carried in air, $U_{\text{in}} = 100 \text{ cm s}^{-1}$, $T_{\text{in}} = 47 \text{ }^\circ\text{C}$, and $p = 1 \text{ atm}$	34
Figure 4.4	Solution profiles for 50 micron droplets with equal proportion of composition of heptane, dodecane, and tetradecane carried in air, $U_{\text{in}} = 200 \text{ cm s}^{-1}$, $T_{\text{in}} = 500 \text{ }^\circ\text{C}$, and $p = 10 \text{ atm}$	35
Figure 4.5	Comparison of the solution profiles for the inlet droplet diameters: 10, 20, 30, and 50 μm . The liquid fuel mixture at the inlet is C_7H_{16} , $\text{C}_{12}\text{H}_{26}$ and $\text{C}_{14}\text{H}_{30}$ with equal mole percentage. The inlet drop temperature $T_{d_0} = 47 \text{ }^\circ\text{C}$. The gas composition at both injectors is air with $U_{\text{in}} = 200 \text{ cm s}^{-1}$, $T_{\text{in}} = 500 \text{ }^\circ\text{C}$, and $p = 10 \text{ atm}$	37
Figure 4.6	Comparison of the solution profiles for the inlet droplet diameters: 10, 20, 30, and 50 μm . The liquid fuel mixture at the inlet is C_7H_{16} , $\text{C}_{12}\text{H}_{26}$ and $\text{C}_{14}\text{H}_{30}$ with equal mole percentage. The inlet drop temperature $T_{d_0} = 47 \text{ }^\circ\text{C}$. The gas composition at both injectors is air with $U_{\text{in}} = 200 \text{ cm s}^{-1}$, $T_{\text{in}} = 700 \text{ }^\circ\text{C}$, and $p = 10 \text{ atm}$	38

Figure 4.7 Comparison of the solution profiles for the inlet droplet diameters: 10, 20, 30, and 50 μm . The liquid fuel mixture at the inlet is $\text{C}_{12}\text{H}_{26}$, $\text{C}_{14}\text{H}_{30}$, and $\text{C}_{16}\text{H}_{34}$ with equal mole percentage. The inlet drop temperature $T_{d_0} = 47^\circ\text{C}$. The gas composition at both injectors is air with $U_{\text{in}} = 200 \text{ cm s}^{-1}$, $T_{\text{in}} = 500^\circ\text{C}$, and $p = 10 \text{ atm}$ 40

Figure 4.8 Comparison of the solution profiles for the inlet droplet diameters: 10, 20, 30, and 50 μm . The liquid fuel mixture at the inlet is $\text{C}_{12}\text{H}_{26}$, $\text{C}_{14}\text{H}_{30}$, and $\text{C}_{16}\text{H}_{34}$ with equal mole percentage. The inlet drop temperature $T_{d_0} = 47^\circ\text{C}$. The gas composition at both injectors is air with $U_{\text{in}} = 200 \text{ cm s}^{-1}$, $T_{\text{in}} = 700^\circ\text{C}$, and $p = 10 \text{ atm}$ 41

LIST OF TABLES

Table 3.1	Planck mean absorption coefficients	16
Table 4.1	Droplet compositions at the inlet	30
Table 4.2	Baseline inlet parameters	34

ACKNOWLEDGMENTS

I am very grateful to Dr. Kee for the two years spent working with me. Dr. Kee has always been very supportive and eager to explain difficult concepts. I would also like to acknowledge Dr. Zhu for helping explain physical concepts and giving insights into modeling. I am appreciative of Dr. Dean for serving on my thesis committee. This effort was supported by the Office of Naval Research via Grant N00014-08-1-0539.

CHAPTER 1

INTRODUCTION

A wide range of combustion technology uses liquid fuels, often introduced as a spray of droplets. Following droplet vaporization, gas-phase combustion can proceed in the surrounding oxidizing environment. Understanding the droplet vaporization process is a central aspect of understanding the overall combustion process. For example, vaporization characteristics affect the local fuel-air equivalence ratio at the point of combustion, which, in turn, affects burning velocities, combustion efficiency, and pollutant emissions.

Droplet vaporization has been studied extensively for decades, both experimentally and theoretically, with excellent texts, monographs, and reviews being available [20, 21, 26, 34, 38, 46, 53]. Nevertheless, there remain important aspects that merit continued research. The present research is motivated particularly by a need to understand multicomponent fuel mixtures, including synthetic fuels and blends.

The physical properties (e.g., vapor pressure, latent heat, density, and heat capacity) can vary greatly between different fuels, causing the droplet vaporization process to be significantly affected by the particular fuel mixture. Because certain species vaporize significantly faster than other species, the both the droplet composition and the surrounding gas-phase composition can vary greatly during the vaporization process. In addition to the droplet's initial composition and diameter, the vaporization process is significantly affected by the temperature, pressure, velocity, and composition of the local gas-phase flow field.

The interaction of a fuel spray with the surrounding three-dimensional turbulent flow field within a practical combustion chamber is extraordinarily complex. An important objective of the present investigation is to model droplet vaporization in a much simpler flow field, but one that shares some of salient characteristics of the

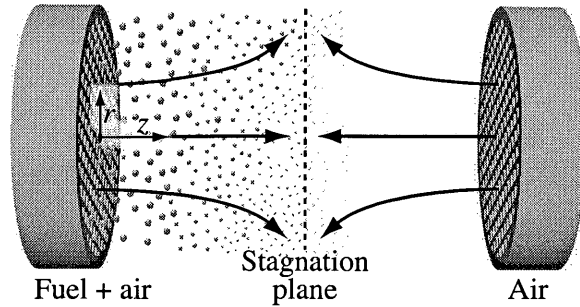


Figure 1.1: Opposed flow liquid fuel droplet vaporization configuration.

practical situation. This approach enables a basic study of the vaporization process, which can be isolated from the practical complexities that sometimes frustrate a fundamental understanding. However, it is important to derive quantitative insights that can be beneficially applied to the design and development of practical systems.

As illustrated in Figure 1.1, an opposed stagnation flow is chosen for present study. In this configuration, droplets are introduced with a carrier gas from the lower manifold. The carrier gas may be inert or may contain some oxygen. The opposed flow is typically an oxidizer species, such as air. By varying the inlet velocities the local fluid-mechanical strain field can be varied, which can affect vaporization. Varying the temperatures of the inlet gas streams has a large effect on vaporization rates. The operating pressure can be varied as well. Although Figure 1.1 shows a flame and the model itself is written to accommodate combustion chemistry, the present study considers vaporization alone without combustion.

Although the flow field is axisymmetric and two-dimensional, it can be shown that because of stagnation-flow similarity the mathematical formulation can be reduced to a one-dimensional boundary-value problem [25]. It can also be shown that with only minor restrictions the droplet trajectories also follow the similarity. The mathematical simplifications lead to efficient computational solution algorithms, which thus enable extensive parameter studies or include other complicated submodels into the present model.

This thesis presents results of studies for three different fuel mixtures. The first involves a heptane-ethanol droplets, which is motivated by applications for direct-injection spark-ignition (DISI) engines. In this application, the droplets are injected at the beginning of the compression stroke when temperature and pressure are low. A second set of studies involves mixtures of heptane, dodecane, and tetradecane. These studies are motivated by applications in diesel engines using alternative and synthetic fuels. At third set of studies, also motivated by diesel applications, involves fuel mixtures of dodecane, tetradecane, and “diesel fuel.” In this case, realistic physical properties are used for the liquid diesel fuel, but the gas-phase vapors from the diesel are assumed to be those of $C_{16}H_{34}$. In the later two cases, the droplets are introduced into a relatively high temperature (up to 700 °C) and high pressure (up to 10 atm.) flow field.

The results of the parameters studies show effects of droplet size and composition, on the vaporization characteristics and the surrounding gas-phase flow field. As might be anticipated, highly volatile compounds such as heptane or ethanol vaporize more quickly than the higher alkanes. Consequently, the droplet composition tends toward higher fractions of the higher alkanes during its lifetime. The local gas-phase fuel-air equivalence ratios are also affected by the differential vaporization rates of the droplet components. As is also anticipated, larger droplets vaporize slower than smaller droplets. Droplet also vaporize faster in higher temperature flow fields. The parameter studies reported here quantify the effects of a wide range of droplet and flow-field parameters.

CHAPTER 2

LITERATURE REVIEW

As one of the important steps of the combustion processes of the liquid fuels, the evaporation of the liquid droplets have been widely studied to fully understand the physicochemical mechanism of liquid fuel spray combustion. The investigation of the droplet vaporization mechanism and characteristics can be used to design and optimize the combustors. Stefan was the first one to use the experiment to systematically investigate the evaporation phenomena [42]. In this experiment, the liquid is maintained at a fixed height in a narrow tube while a different gas flow crosses the open top of the tube. The liquid inside the tube evaporates to the gas flows. Stefan pointed out that the driving force for the evaporation is mainly the mass diffusion. And the evaporation rate of the liquid is inversely proportional to the distance of the liquid-gas interface to the open end of the tube. This cornerstone experiment for the liquid vaporization is called Stefan problem. Hertz found that the evaporation rate for any liquid substance is strongly related to the temperature at the liquid-gas interface, and is determined by the temperature-dependent equilibrium vapor pressure.

Godsave [17] established the fundamental principles for single-component hydrocarbon vaporization and combustion in an oxidizing atmosphere. In this experiment, a single droplet with original diameter of approximately 0.15 cm was suspended on a fine silica filament for combustion at temperature of 100-120 °C and the droplet diameter was photographed at approximately 0.25 second intervals. Based on the observation of the variation of the droplet diameter, two distinct mechanisms were proposed for the processes of evaporation and combustion of the droplet. If the droplet temperature is almost the same as that of the ambient atmosphere, the evaporation rate of the droplet is determined mainly by diffusion processes. On the other hand,

if the temperature difference between the droplet and the surrounding atmosphere is large, the vapor heat content at the boiling point is the important factor on for droplet evaporation process.

Nishiwaki [32] experimentally studied the evaporation and ignition lag of fuel droplets at various ambient air temperature. A fuel droplet was suspended on a silica filament and put into the combustion chamber quickly. An Optical system was set up to obtain droplet evaporation rate. The experimental results showed that the square of the diameter varies linearly with time during the processes of evaporation and combustion, which is now called d^2 -law. Based on the study of single component droplet combustion in a stagnant oxidizing atmosphere, Godsave [17], Wood et al. [50], and Williams et al. [49] established the principal approach to investigate the droplet evaporation that could lead to the d^2 -law. Turns [45] systemically derived the d^2 -law of evaporation based on the mass conservation equation with certain assumptions. Though the d^2 -law was not held during the initial transient period of the evaporation, it is a fundamental criterion for droplet evaporation.

Williams [47] developed a comprehensive theory on spray combustion in 1959. It becomes necessary to couple the fluid motion equation and spray equation when solving practical spray combustion problems because the interaction between spray and the surrounding fluid is often very important. Starting from the derivation of motion governing equations, Williams obtained the simplified one-dimensional flow equations with a heterogeneous burning-velocity eigenvalue problem. Williams's spray theory laid a good foundation for studying on spray evaporation. Williams [48] established a theory on statistical description of spray-combustion processes which could be widely used in practical applications. And he studied the dilute sprays through driving a statistical governing equation based on the knowledge of detailed properties of single droplets. Iterative numerical method was applied to solve the coupled equations of spray governing equation and fluid dynamical equations. The interactions between

the collision droplets were examined as a illustration of the importance of specific effects. Williams also built a idealized model of impinging jet atomization to inspect and verify his spray theory. He then discussed the behavior of sprays composed of very small particles and focused on one-dimensional steady-state laminar flow of burning sprays. Finally, he proved his spray theory could be widely used in variety of spray-combustion problems by examining rocket-chamber combustion. Williams's work provided an important theoretical support for further investigations of evaporation and burning mechanism. Based on his theoretical principles, advanced researches including interactions of colliding droplets, turbulent combustion, and internal combustion engine detonation problems were prosperously developed.

For the single-component non-dilute droplet spray, the evaporation of droplet spray behaves in a different manner from the evaporation of single droplets. To obtain a clear knowledge of droplet spray evaporation, Bellan and Cuffel [5] developed a theory of evaporation of mono-disperse single-component non-dilute spray based on conservation laws by taking into account interactions between droplets. Bellan and Cuffel [5], Bellan and Harstad [6] studied the convective evaporation of non-dilute clusters of droplets. They built a model of convective droplet-cluster evaporation based on the consideration of influence of outer flow on the cluster of droplets, and pointed out that the initial relative velocity between droplet cluster and the ambient atmosphere was not a significant controlling parameter and the initial ambient temperature was really important especially when the droplet cluster was in a ambient of temperature of 750 – 1500 K. Results showed that when the penetration distance of outer flow to the cluster volume is relatively small, the theory was valid for very dense clusters. Bellan and Harstad [7] built a global model to research the convective evaporation of dense and dilute clusters of droplets, and pointed out that for dense spray in low temperature regime, the most important control parameter is the initial temperature of droplet, and the following is the initial ambient temperature. The

initial mass fraction of fuel vapor in the gas phase and the initial velocity between droplets and ambient gas are relatively weak control parameters. In the dilute spray case, in a significant low temperature system, the initial temperature of the ambient gas was the dominant influence factor and the initial relative velocity between droplets and gases followed. Initial droplet temperature and mass fraction of fuel in the ambient gas are relatively weak influence factors.

Law et al. [27] analyzed the evaporation of multi-component droplet in a convective ambient. They studied both thermal and fluid mechanical behaviors of multi-component droplet vaporization considering internal circulation through the droplet surface shear and its effects on heat and mass transport of the droplet. Transient behavior of droplet evaporation was examined by building a more complicated model considering the potential flow, Hill's Vortex and boundary layer influence. However, only one droplet evaporation and combustion circumstance is considered. Urbaneja and Sirignano [36] analyzed multi-component droplet at high Reynolds number. It, however, still did not lead to the droplet spray evaporation. Williams and Sirignano [39] analyzed the droplet vaporization in a hot ambient and spray combustion, and considered multi-component fuel and fuel groups vaporization and sprays, and showed that relative velocity between droplets and ambient gas had important influence on vaporization rate. Although a general theory of fuel droplet vaporization and spray combustion was presented, the interaction between droplets in a spray was not included. Williams and Sirignano's work was a good foundation for the following studies of droplet spray vaporization and combustion, although there are still simplifications, like interactions between droplets are not well studied. The models from Bellan and Cuffel [5] could be used to improve Williams and Sirignano's theory.

After a comprehensive study of single aerosol particle in 1981 [12], Ravindran and Davis [15] analyzed single charged two-component droplets. In their paper, a single electrostatic droplet was suspended and its evaporation rates were measured. The

measurements were compared with the diffusion-controlled evaporation model of a binary ideal solution. Their main contribution was that an experiment was set up to measure the droplet evaporation using light scattering technique.

In 1989, Abramzon and Sirignano [1] developed a computational algorithm for multi-component droplet spray combustion calculations. They improved the classical model by including many effects, such as thermophysical properties, non-unitary Lewis number in the gas phase, Stefan flow on heat and mass transfer and internal circulation and transient liquid heating. Droplet dynamics and gas-phase theory were introduced. The gas phase simulation, which had included the Stefan flow effects in the liquid-gas interface, were based on the classical film theory. The liquid droplet was assumed to be spherical in the heating and evaporation processes. The model could be used in droplet spray evaporation and combustion calculations with large amount droplets.

Since the real industrial fuels consist of a huge number of components, continuous multi-component (CMC) approach and discrete multi-component (DMC) fuel method were developed to represent real fuels. The development of continuous multi-component approach is based on continuous thermodynamics method [44], which describes the droplet component as a distribution function and the parameter of the distribution function was solved numerically. The commonly used distribution function is gamma distribution function and the parameter is the molecular weight. The advantage of CMC method is that it can significantly reduce the computational cost without losing the complexity of actual situation of multi-component droplet evaporation. But the disadvantage is that it is not very applicable to combustion simulations with detailed chemical kinetics [34] because it is difficult for CMC method to describe multi-component features of each individual component. The DMC method was commonly used both in the early stages and nowadays because this approach has higher precision, especially when the number of component of a droplet is relatively small.

Moreover, DMC approach enables coupled reaction kinetics of individual component when considering the situation of multi-component droplet evaporation. A major drawback of DMC method, however, is that it would find itself powerless in the face of droplet evaporation situation with significantly large amount components. With the rapid development of computer technology and improvement of computational algorithm, it is reasonable to believe that the DMC approach will play a greater and greater role in the computing field of multi-component evaporation.

Both CMC and DMC approaches have advantages and disadvantages. Alternative choice would combine DMC and CMC approaches to predict the physical properties of fuels. Zhang and Kong [53] studied single droplet vaporization process using both DMC and CMC models. Biodiesel, diesel-biodiesel and gasoline-ethanol are investigated. The DMC model was used to represent biodiesel, which is divided into five major components. The overall properties of biodiesel fuel are evaluated under reduced temperature, pressure and volume. Hybrid of DMC and CMC method was used to simulate the evaporation situation of gasoline-ethanol droplets because ethanol was considered as a pure single-component fuel while the components of gasoline were described by a gamma distribution function.

In 2002, Burger et al. [8] introduced the Distillation Curve model (DC model), which is more computationally effective to deal with multi-component droplet evaporation. DC model assumes an algebraic relationship between the vapor molecular weight and the vaporized mass fraction, by which the properties of the vapor can be determined [52].

The present study uses the discrete components approach to investigate the vaporization behaviors of droplets containing several components under the operating conditions of the diesel engine combustion. The droplet vaporization model is incorporated into the axisymmetric opposed stagnation flow as illustrated in Figure 1.1 [25]. This flow configuration was chosen for several reasons: it is well defined and has

been examined both experimentally and numerically; and it allows the decoupling of droplet-droplet and droplet-gas interactions from calculation complications [10]; moreover, it can represent strain-rate effects in a very well defined flow field. Continillo and Sirignano showed that stagnation-flow similarity is valid for two-phase situation with liquid fuel droplets [11]. Li [29] reported an elaborate explanation of applications of stagnation flow in various spray structures. Although the opposed stagnation-flow is ideal, it is very useful to study the effects of fluid mechanical strain on flame behavior in practice [25] and the results can assist characterizing turbulent spray combustion via laminar flamelet models.

The opposed stagnation flow with droplet vaporization has been studied both experimentally and numerically. Chen and Gomez [10] experimentally investigated the structure of counterflow diffusion flames. They measured the variation of the droplet size, velocity and gas-phase temperature in different flames and studied the effects of the strain rate on flame structure, and pointed out that for a mono-disperse spray evaporation, the droplet size distribution will generally extend in width due to the size-dependent evaporation rate. Continillo and Sirignano [11] developed the counterflow spray combustion model and studied the influences of initial droplet diameter, strain rate, mass fraction and temperature on the flame structure. Lentati and Chelliah [28] used the numerical model to study flame-extinction characteristics in opposed-flow flames with the assumption of quasi-steady mono-disperse spray conditions. Kee et al. [21] generally followed the same approaches but with different computational algorithm, and studied the effects of liquid-fuel thermophysical properties, carrier-gas composition, and pressure, on strained opposed-flow non-premixed flames. The present study extends the computational algorithm reported in [21] to consider the multi-component liquid-fuel droplets.

CHAPTER 3

MODEL DEVELOPMENT

Figure 1.1 shows the geometric configuration of the axisymmetric opposed stagnation flow. It consists of two concentric, circular nozzles directed towards each other, and produces an axisymmetric flow field with a stagnation plane between the nozzles. The location of the stagnation plane depends on the momentum balance of the two streams. The liquid-fuel droplets are introduced at the left-hand side carried by the air, and the air is injected at the right-hand nozzle. The opposed-flow geometry makes an attractive experimental configuration since the two-dimensional flow can be reduced to one dimension based upon similarity and assumption that the radial velocity varies linearly in the radial direction. It leads to a simplification in which the fluid properties are functions of the axial distance only.

This configuration was used to simulate the droplet spray vaporization in an internal combustion engine. In practical premixed combustion chamber of the diesel engine, liquid fuel and air are injected into a mixer from feeder nose separately, and then fuel-air mixture is sprayed into combustion chamber. The fuel-air mixture flow in the combustion engine during a compression stroke may be described by droplet spray in a stagnation flow configuration.

As the droplets approach to the stagnation plane, where the temperature is high due to the impingement of opposed high temperature flowing air, droplets become smaller and smaller because of vaporization. Depending upon flow conditions and fuel characteristics, the droplets may be completely vaporized before entering the stagnation plane. If the droplet diameter is large enough or droplets contains heavy components which are not easy to vaporize, the droplet may go across the stagnation plane and even vibrate around the stagnation plane before vaporizes completely. In this case, it is expected that the droplet temperature increases very fast and mole

fractions of gas-phase components of the droplet are higher than other position in the flow field because most of the droplet vaporizes there. It is easy to understand the reason for the expectation. Larger and less volatile droplet will survive to the stagnation plane where blowing forces from both side keep the droplet relative equilibrium there until the remaining part of the droplet vaporizes completely. Besides, since a relatively large amount droplet vaporization in a small local position, the mole fractions of gas-phase droplet components and the temperature of the droplet near the stagnation plane are higher than other positions in the flow field. It should also be noticed that, although droplet vaporization leads to an increase in gas-phase droplet components, gas-phase droplet components are blown away at the same time. An accumulation of vaporization near the stagnation plane for large and less volatile droplets results in the highest mole fractions of droplet components.

To understand the droplet vaporization processes and its interaction with the strained fluid flow, this study assumes that the liquid-fuel droplets issuing from the nozzle have the same size. To reduce the mathematical complication, the slip effects are negligible based on the assumption that the fuel droplets are in dynamical equilibrium with their host environment. The fuel droplets evaporates in an inert environment and the droplet shape remains spherical during vaporization. It is also assumed that the multicomponent fuel mixture within the droplet is well mixed during the entire vaporization processes. The Euler approach is used to describe the opposed stagnation flow, while the Lagrangian dynamic approach is used to represent the movement of the droplets within the flow field. This computational solution method is implemented as an iterative algorithm between Eulerian gas-phase conservation equations and Lagrangian droplet tracking [28]. The gas-phase conservation equations incorporate source terms for droplet mass, momentum, energy, and species mass that are associated with the droplet motion and vaporization. As the droplets travel through the gas-phase flow, their behavior is directly influenced by the local

gas phase composition.

3.1 Eulerian Gas-phase Conservation Equations

Using the similarity approximation, the governing equations for steady, laminar, axisymmetric opposed flow [1, 19, 21, 25, 28, 31, 40] can be extended to incorporate source terms associated with droplet motion and vaporization as follows:

$$\frac{d(\rho u)}{dz} + 2\rho V = S_M, \quad (3.1)$$

$$\rho u \frac{dV}{dz} + \rho V^2 = -\Lambda_r + \frac{d}{dz} \left(\mu \frac{dV}{dz} \right) + S_V - V S_M, \quad (3.2)$$

$$\begin{aligned} \rho \sum_{k=1}^K (u + V_k) Y_k c_{pk} \frac{dT}{dz} &= \frac{d}{dz} \left(\lambda \frac{dT}{dz} \right) \\ - \sum_{k=1}^K \dot{\omega}_k W_k h_k - Q_{\text{rad}} + S_T - \sum_{k=1}^K h_k S_k, \end{aligned} \quad (3.3)$$

$$\rho u \frac{dY_k}{dz} + \frac{d(\rho Y_k V_k)}{dz} = \dot{\omega}_k W_k + S_k - Y_k S_M. \quad (3.4)$$

In the optically thin limit, radiation transfer between gaseous species in the flame and the environment can be approximated as [3],

$$Q_{\text{rad}} = \varepsilon \sigma (T^4 - T_\infty^4), \quad (3.5)$$

where σ is the Stefan-Boltzmann constant and T_∞ is the environment temperature. The apparent emissivity is evaluated as $\varepsilon = 4 \sum_k p_k \zeta_k$ where p_k and ζ_k are gas-phase partial pressures (atm) and the Planck mean absorption coefficients ($\text{atm}^{-1} \text{m}^{-1}$), respectively. Only H_2O and CO_2 are considered here, and their Planck mean absorption coefficients are evaluated as polynomials

$$\zeta_k = \sum_{n=0}^5 c_{k,n} \left(\frac{1000}{T} \right)^n. \quad (3.6)$$

The coefficients c_n are given in Table 3.1 [3].

The independent variable is the axial coordinate z . The dependent variables are axial velocity u , scaled radial velocity $V = v/r$ where v is the radial velocity and r is the radial coordinate, temperature T , and species mass fractions Y_k . The pressure

Table 3.1: Planck mean absorption coefficients

	H ₂ O	CO ₂
c_0	-0.23093	18.741
c_1	1.12390	-121.310
c_2	9.41530	273.500
c_3	-2.99880	-194.050
c_4	0.51382	56.310
c_5	-1.86840E-5	-5.8169

gradient term, $\Lambda_r = (1/r)(dp/dr)$, is an eigenvalue. The mass density is evaluated with an ideal-gas equation of state. The diffusion velocities V_k depend upon gradients of composition and temperature, representing both ordinary multicomponent diffusion and thermal diffusion [25]. The molar production rates of species by chemical reaction are represented as $\dot{\omega}_k$. Transport properties include mixture viscosity μ and thermal conductivity λ . All properties and reaction rates are evaluated through CHEMKIN interfaces [25]. Source terms for total mass S_M , mass for species S_k , radial momentum S_V , and thermal energy S_T are associated with fuel droplets.

As illustrated in Figure 1.1, $z = 0$ is at the lower inlet manifold where the droplets are introduced and the upper boundary is at $z = L$. Boundary conditions at both manifolds are required. The velocity and temperature at $z = 0$ may be specified as,

$$u = U_{\text{in}}, \quad V = 0, \quad T = T_0. \quad (3.7)$$

The species boundary condition is

$$\dot{m}'' \epsilon_{k,0} = \dot{m}'' Y_k + \rho Y_k V_k, \quad (3.8)$$

where $\dot{m}'' = \rho U_{\text{in}}$ is the total mass flux and mass-flux fractions $\epsilon_{k,0}$ are specified. The boundary conditions for the opposing flow at $z = L$ are analogous.

3.2 Lagrangian Droplets Dynamics

The droplet with multicomponent species is assumed to be well mixed such that there does not exist temperature and composition gradients within the droplet. The Lagrangian equations that track droplet motion and vaporization are summarized as

$$\frac{dz_d}{dt} = u_d, \quad \frac{dr_d}{dt} = r_d V_d, \quad (3.9)$$

$$\frac{dm_d}{dt} = \dot{m}_d, \quad (3.10)$$

$$\frac{du_d}{dt} = \frac{F_z}{m_d}, \quad \frac{dV_d}{dt} = -V_d^2 + \frac{F_r}{m_d r_d}, \quad (3.11)$$

$$\frac{dT_d}{dt} = \frac{\dot{q}_d}{m_d c_{pd}}, \quad (3.12)$$

$$\frac{dY_{d,k}}{dt} = \frac{\dot{m}_d}{m_d} (\epsilon_k - Y_{d,k}), \quad (3.13)$$

$$\frac{d\mathcal{F}}{dt} = -2\mathcal{F}V_d. \quad (3.14)$$

The independent variable is time t . The dependent variables are the droplet's axial position z_d , radial position r_d , mass m_d , axial velocity u_d , scaled radial velocity $V_d = v_d/r_d$, temperature T_d , mass fractions $Y_{d,k}$, and the droplet flux-fraction function \mathcal{F} . The droplet's mass and diameter d are related as $m_d = \pi\rho_d d^3/6$. The axial force F_z considers drag and thermophoresis. Because of similarity, the radial force F_r considers only drag. Heat transferred from the gas to the droplet is \dot{q}_d and droplet heat capacity is c_{pd} . The total mass vaporization rate is denoted as \dot{m}_d , and the fraction of the mass vaporization rate for k -th species is denoted as $\epsilon_k = \dot{m}_{d,k}/\dot{m}_d$. Droplet behavior depends upon the local gas-phase environment, which is interpolated from the gas-phase solution. Solution to the Lagrangian initial-value problem requires initial values of all dependent variables at the droplet inlet ($z = 0$).

The droplet flux-fraction function \mathcal{F} is defined as the ratio of the number of droplets crossing a unit surface area perpendicular to the z -axis at time t and the number of droplets crossing an equivalent area at time t_0 [28]. Stagnation-flow similarity requires that all the droplets crossing an inlet area A_0 at time t_0 will also cross a parallel area A_t at time t . Thus, the function \mathcal{F} may be equivalently defined as $\mathcal{F} = A_0/A_t$. By definition, at the inlet manifold (initial condition) $\mathcal{F} = 1$. Because the droplets spread radially, $\mathcal{F} \leq 1$.

3.3 Droplet Vaporization

During the vaporization processes of a liquid droplet, the spatial domain can be divided into three zones [33]. The first zone is the interior of the liquid droplet, where heat and mass are transported due to the gradients of the temperature and the species concentrations. Because the most volatile component vaporizes fast, the droplet composition varies during droplet lifetime. The second one is the droplet surface, where liquid and gas phase reach a equilibrium state governing by vapor pressure equation. And the third one is the surrounding gas phase, where heat and mass exchanges between the droplet and the environment occur.

There are three types of models with different levels of complexity for estimating the droplet vaporization rate. The first one is called rapid-mixing model (RMM), which assumes that the diffusion resistance within the droplet is zero. RMM is applied for slow evaporation processes when droplet internal heat conduction and mass diffusion has little effects on internal temperature and concentration. The second one is called thin-skin model (TSM), which is also known as thin-film model. TSM assumes a infinite diffusion resistance so that droplet temperature and concentrations are unchanged during the vaporization process, and heat and mass transfer occur only within a thin film on the droplet surface. The third one is called diffusion-limit model (DLM). DLM resolves the temperature and concentration profiles inside the droplet. Though DLM may be more accurate, it needs much more computational cost. In this study, the thin-film assumption that considers transport through a vapor-phase boundary layer surrounding a droplet is used to evaluate the droplet vaporization rate and heat exchange with the droplet environment [1, 19, 40, 41].

In calculating the total mass evaporation rate of the multicomponent droplet, \dot{m}_d , the mixture of the vapor species is lumped as a single vapor species, and its mass fraction on the droplet surface and in the environment is defined as

$$Y_{v,s} = \sum_k Y_{v,s,k} \quad (3.15)$$

$$Y_{v,g} = \sum_k Y_{v,g,k} \quad (3.16)$$

where $Y_{v,s,k}$ and $Y_{v,g,k}$ are the mass fractions of the vapor species mixture on the droplet surface and in the gas far from the droplet, respectively, and the summation is over all the vapor species only.

Droplet evaporation rate is calculated using a modified Sherwood number Sh_v^* as

$$\dot{m}_d = -\pi d \rho_f D_{v,f} Sh_v^* \ln(1 + B_v), \quad (3.17)$$

where ρ_f is the film density and $D_{v,f}$ is the vapor diffusion coefficient within the film. The modified Sherwood number $Sh_v^* = 2 + (Sh_0 - 2)/F(B_v)$ considers the change of the film thickness due to Stefan flow using the function $F(B_v) = (1 + B_v)^{0.7} \ln(1 + B_v)/B_v$, where B_v is the overall Spalding mass-transfer number defined as,

$$B_v = \frac{Y_{v,s} - Y_{v,g}}{1 - Y_{v,s}}. \quad (3.18)$$

For non-evaporating droplets

$$Sh_0 = 2 + 0.552 Re_d^{1/2} Sc^{1/3}, \quad (3.19)$$

where the Schmidt number is $Sc = \mu_f/(\rho_f D_{v,f})$ and μ_f is the viscosity of the film mixture. The droplet Reynolds number is defined as

$$Re_d = \rho_f |\mathbf{v} - \mathbf{v}_d| d / \mu_f, \quad (3.20)$$

where \mathbf{v} and \mathbf{v}_d are the local gas-phase and droplet velocities, respectively.

Droplet vaporization is assumed to be sufficiently fast that the vapor concentration at the droplet surface is saturated. Thus, the mole fractions of the vapor on the droplet surface can be calculated as,

$$X_{v,s,k} = X_{d,k} p_{v,k} / p, \quad (3.21)$$

where $p_{v,k}$ is the saturation vapor pressure of the k -th pure species at the droplet temperature of T_d , $X_{d,k}$ is the mole fraction of k -th species of the liquid-phase mixture of the droplet, and p is the local gas pressure.

The vaporization rate of individual species $\dot{m}_{d,k}$ is estimated using the mass fraction of the vaporizing species ϵ_k as $\dot{m}_{d,k} = \dot{m}_d \epsilon_k$, while the mass fraction ϵ_k is calcu-

lated based on the definition of the Spalding mass transfer number for each individual species B_k as,

$$\epsilon_k = Y_{v,s,k} + (Y_{v,s,k} - Y_{v,g,k}) / B_k. \quad (3.22)$$

The Spalding mass transfer number for each individual species B_k may be estimated based on B_v as [35, 46],

$$B_k = (1 + B_v)^{\eta_k} - 1. \quad (3.23)$$

where $\eta_k = D_{v,f} / D_{k,f}$.

3.3.1 Droplet Heat Transfer

Heat transferred from the gas into the droplet is estimated as

$$\dot{q}_d = -\dot{m}_d \left[\frac{c_{p,v} (T - T_d)}{B_T} - L_v \right], \quad (3.24)$$

where B_T is the Spalding heat-transfer number, and is related to Spalding mass-transfer number B_v as

$$B_T = (1 + B_v)^\phi - 1, \quad (3.25)$$

where

$$\phi = \frac{c_{p,v} \text{Sh}_v^*}{c_{p,f} \text{Nu}^*} \cdot \frac{1}{\text{Le}_f} \quad (3.26)$$

The mean latent heat L_v of vaporization can be represented as

$$L_v = \sum_k \epsilon_k L_{v,k}(T_d) \quad (3.27)$$

where $L_{v,k}(T_d)$ is the latent heat of vaporization of the k -th species at the droplet temperature T_d . $c_{p,f}$ is the film mixture heat capacity. The heat capacity of the vapor mixture in the film $c_{p,v}$ is calculated as

$$c_{p,v} = \sum_k \epsilon_k c_{p,v,k}. \quad (3.28)$$

Nu^* is a modified Nusselt number (analogous to Sh_v^*), and Le_f is the Lewis number within the film. The film Lewis number is defined as $\text{Le}_f = \alpha_f / D_{v,f}$, where α_f is the thermal diffusivity of the gas in the film and $D_{v,f}$ is the mixture-averaged diffusion coefficient of the vapor species in the film. Establishing consistent values of \dot{m}_d , B_v

and B_T , and thus evaluating \dot{q}_d , is an iterative process [1].

3.3.2 Droplet Momentum

Droplet-momentum conservation is written as

$$\frac{d(m_d \mathbf{v}_d)}{dt} = \dot{m}_d \mathbf{v}_d + \mathbf{F}. \quad (3.29)$$

Relevant forces include shear drag \mathbf{F}_D and thermophoresis \mathbf{F}_T . The drag force \mathbf{F}_D is expressed in terms of the drag coefficient as

$$\mathbf{F}_D = \frac{1}{2} \rho_f C_D A_d |\mathbf{v} - \mathbf{v}_d| (\mathbf{v} - \mathbf{v}_d). \quad (3.30)$$

where $A_d = \pi d^2/4$ is the droplet projected area. The drag coefficient C_D is [1],

$$C_D = \frac{24}{\text{Re}_d} \left[1 + \frac{\text{Re}_d^{2/3}}{6} \right]. \quad (3.31)$$

The thermophoretic force due to the gas-phase temperature gradient can be represented as [43, 51]

$$\mathbf{F}_T = -\frac{3\pi d \mu_f^2 K_T \nabla T}{\rho_f T}. \quad (3.32)$$

where the thermophoretic coefficient K_T depends on the properties of both the gas-phase mixture and the droplet, and may be expressed as [43],

$$K_T = \frac{2C_s [(\lambda_f/\lambda_d) + C_t \text{Kn}]}{(1 + 3C_m \text{Kn}) [1 + 2(\lambda_f/\lambda_d) + C_t \text{Kn}]}. \quad (3.33)$$

Here, λ_d is the thermal conductivity of the droplet. The order-unity constants C_s , C_t , and C_m are the thermal creep, temperature jump, and velocity jump coefficients due to the noncontinuum effects at the droplet-gas interface, respectively, have values of $C_s = 1.147$, $C_t = 2.20$, and $C_m = 1.146$ [4]. The Knudsen number Kn is defined as the ratio of the gas-phase mean free path length ℓ_f to the droplet radius, $\text{Kn} = 2\ell_f/d$. The mean free path length ℓ_f can be calculated as $\ell_f = \mu_f/\phi\rho_f c_g$, where the mean molecular speed c_g is estimated as $c_g = \sqrt{8RT/\pi\bar{W}}$, and the dimensionless parameter $\phi = 0.491$ is adopted from Allen and Raabe [2]. Because radial temperature gradients vanish (similarity assumption), the thermophoretic force is only axial.

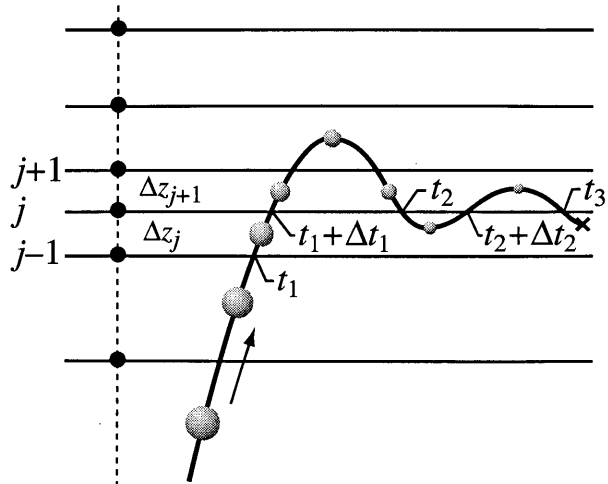


Figure 3.1: Illustration of evaporating droplet motion, crossing the Eulerian mesh boundaries.

3.3.3 Gas-phase Source Terms

The interaction between the gas-phase and the droplets is represented in terms of mass, momentum, and energy sources S_M , S_V and S_T in Eqs. 3.1-3.4. Sources for individual droplets are represented as

$$\mathbf{s} = \begin{pmatrix} s_M \\ s_k \\ s_V \\ s_T \end{pmatrix} = - \begin{pmatrix} \dot{m}_d \\ \dot{m}_d \epsilon_k \\ \dot{m}_d V_d + F_r / r_d \\ \dot{m}_d \sum_k \epsilon_k h_{d,k} + \dot{q}_d \end{pmatrix}, \quad (3.34)$$

where the right-hand sides are evaluated from solutions of the Lagrangian droplet dynamics. The liquid-phase specific enthalpy of the droplet species is evaluated as $h_{d,k} = h_{g,k} - L_{v,k}$, where $h_{g,k}$ is the specific enthalpy of the vapor phase. This formulation assures self consistency between the liquid and gas-phase thermodynamics and the latent heat.

Figure 3.1 shows that for any computational control volume Δz_j a droplet may cross its boundaries several times or may be completely vaporized within the volume. Assume that the trajectory of each droplet is divided into intervals $[t_n, t_n + \Delta t_n]$, where Δt_n is the time interval that a droplet spends in control volume Δz_j . The source terms (per unit volume) within the control volume Δz_j can be evaluated

as [28]

$$\mathbf{S}(z_j) = \frac{n_{d0} u_{d0}}{\Delta z_j} \sum_{n=1}^{\mathcal{N}_j} \int_{t_n}^{t_n + \Delta t_n} \mathbf{s} \mathcal{F} dt, \quad (3.35)$$

where \mathcal{N}_j is the number of times for a droplet entering the control volume Δz_j before it is completely vaporized. Certainly, \mathcal{N}_j can be zero if a droplet never enters the control volume Δz_j . Lentati and Chelliah [28] showed that this formulation avoids a singularity associated with droplets crossing the stagnation plane and reversing direction. This formulation also assures mass, momentum, and energy conservation between the gas and liquid phases.

3.4 Gas-phase Kinetics

The results in this thesis only consider the droplet vaporization performance, so that gas-phase kinetics are not included in the model. It should be noticed that, however, gas-phase chemical kinetics need to be included when droplet combustion happened and proper reaction mechanism is necessary for the model.

3.5 Numerical Algorithm

Although the liquid and gas phases are highly coupled, the solution algorithm iterates between solving the gas-phase problem on an Eulerian mesh and Lagrangian droplet dynamics. Each iteration of the gas-phase problem is solved using droplet source terms that were evaluated based upon velocity, temperature, composition profiles from a previous gas-phase solution. Upon convergence of the gas-phase problem (with fixed droplet source terms), the Lagrangian droplet-tracking problem is solved to produce new source terms. The process continues until the changes between iterations becomes sufficiently small.

The gas-phase equations are solved using a modification of OPPDIF [30], which has been extended to incorporate droplet source terms. A hybrid Newton method is implemented with TWOPNT [18, 25], which includes adaptive meshing. The droplet

equations are solved using LIMEX [13]. Each Lagrangian droplet solution must terminate as the droplet vanishes (i.e., becomes extremely small). Because the droplet equations depend upon the surrounding gas phase, the local solution is interpolated from the Eulerian mesh as a function of droplet position. Because of the possibility that the iteration can approach a limit cycle between the gas-phase and droplet solutions, a damping strategy is implemented in which the Eulerian solution that is presented to the Lagrangian droplet problem is averaged between two prior solutions. Further implementation details can be found in Kee et al. [21], where smart methods were applied.

The solution process begins either by solving a purely gas-phase that is expected to produce a solution that resembles the droplet-fueled vaporization field or by restarting from a previously computed droplet vaporization solution with similar operating conditions. The Lagrangian droplet-tracking problem (Eqs. 3.9-3.14) is solved using the gas-phase profiles from the related problem, thus producing a new set of gas-phase source terms (Eq. 3.35). The Eulerian gas-phase problem (Eqs. 3.1-3.4) is then solved newly computed source-term profiles, thus producing new gas-phase profiles.

Because it is necessary to determine very accurately the times at which droplets enter and exit each mesh interval (Figure 3.1), a costly root-finding algorithm is needed. Interestingly, even though the Lagrangian problem appears to be a small system of ordinary differential equations, the computational cost can be greater than the Eulerian boundary-value problem. Consequently, the algorithm is written to allow the adaptive meshing in OPPDIF to proceed, but using fixed source-term profiles. As the mesh is refined, the source profiles must be interpolated onto successively finer mesh intervals.

The adaptive-mesh algorithm causes the number of mesh intervals and mesh sizes to vary, which complicates the interpolation of the droplet source-term profiles. Because a simple interpolation of the source profiles does not guarantee mass, momen-

tum, and energy conservation, the following algorithm is developed. Upon adaptive regridding, assume that the total number of new mesh points is N' and the new mesh-point locations are at z'_i ($i = 1, \dots, N'$). The source terms $\mathbf{S}(z'_i)$ on the new mesh points z'_i must be interpolated from the source terms $\mathbf{S}(z_j)$ on the previous mesh points z_j . The interpolation involves a function $\mathbf{G}(z)$ that is defined to be an accumulation of the source terms along the z -axis. On the previous mesh z_j the function $\mathbf{G}(z)$ is defined as

$$\mathbf{G}(z_j) = \sum_{i=0}^j \mathbf{S}(z_i) \Delta z_i. \quad (3.36)$$

The source terms on the new mesh z'_i are evaluated as

$$\mathbf{S}(z'_i) = \frac{\mathbf{G}(z'_i) - \mathbf{G}(z'_{i-1})}{z'_i - z'_{i-1}}, \quad (3.37)$$

where $\mathbf{G}(z'_i)$ are evaluated using linear interpolation of the function values $\mathbf{G}(z)$ at the previous mesh points z_j .

Once the Eulerian solution is solved on a sufficiently resolved mesh, the source terms need to be re-evaluated from the droplet-tracking problem. With new source terms in hand, the gas-phase problem is solved once again. However, because the droplet source terms are based upon a previous gas-phase solution, the adaptive-mesh algorithm may have added mesh points where they are no longer needed. Thus, between iterations the re-gridding algorithm in OPPDIF is used to remove some mesh points.

Especially at high strain rates and with small droplets, the iteration can approach a limit cycle between the gas-phase and droplet solutions. This problem is avoided with a damping strategy in which the Eulerian solution is based upon source terms that are averaged between two prior Lagrangian droplet solutions.

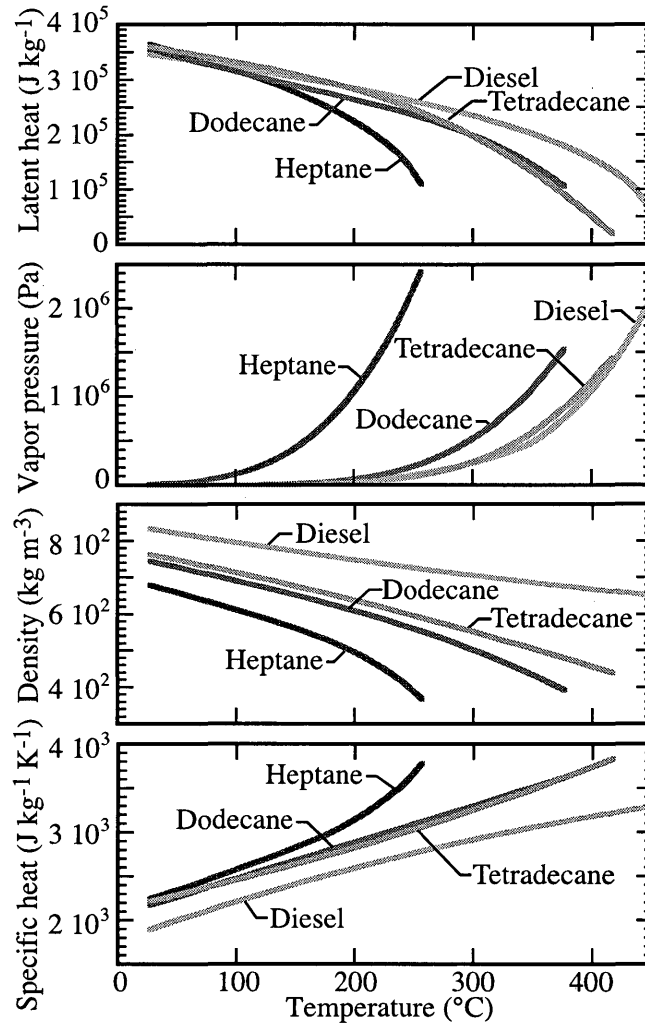


Figure 3.2: Physical properties of liquid heptane, dodecane, tetradecane and diesel.

3.6 Liquid Fuel Properties

Liquid fuels, such as gasoline, diesel, n-alkanes are the major components. Petroleum-derived diesel fuel is a mixture of hydrocarbons with carbon atoms between 8 and 21 per molecule; Commercial gasoline is a mixture of hydrocarbons with carbon chains of 5 to 12 carbon atoms; Jet fuel is a mixture of volatile hydrocarbons with shorter carbon chains of carbon numbers predominantly between 4 and 12. The main component for diesel is n-dodecane, and the main component for gasoline jet fuel is n-octane [9].

The present study considers the fuel mixtures of n-heptane, n-dodecane n-tetradecane, diesel and ethanol to simulate the commercial fuels. Figure 3.2 compares the physical properties: latent heat, vapor pressure, density and specific heat of the liquid fuel components: n-heptane, n-dodecane n-tetradecane and diesel [37]. Figure 3.3 compares the physical properties of n-heptane, methanol and ethanol. The methanol and heptane properties are taken from the NIST Webbook [16] and the ethanol properties are evaluated from Dillon and Penoncello [14]. All liquid properties are fit, usually as high-order polynomials, for evaluation within the modeling software. The ethanol properties span $-23\text{ }^{\circ}\text{C} < T < 240\text{ }^{\circ}\text{C}$, and heptane properties span $-90\text{ }^{\circ}\text{C} < T < 265\text{ }^{\circ}\text{C}$. Gas-phase properties are evaluated from CHEMKIN databases [22–24]. Here, the gas-phase properties of n-hexadecane is used for the diesel. But it should be noticed that in the droplet vaporization model, a mixture of dodecane, tetradecane, and hexadecane was used to represent diesel.

As illustrated in Figure 3.2 and Figure 3.3, the latent heats of droplet components will decrease as temperature increases. Heavier components generally have higher latent heats. Vapor pressure will significantly increase with the increase of temperature. For hydrocarbon of methane series, the heavier the hydrocarbon, the lower the vapor pressure at a specific temperature. Alcohols have higher vapor pressure than n-alkane. Density of liquid hydrocarbons will decrease with the increase of temperature and heavier hydrocarbon has higher density. Specific heat of the hydrocarbons used will increase with the increase of temperature and lighter alkane generally has higher specific heat. Alcohols have higher specific heat than alkanes.

The physical properties of the liquid-fuel components shown in Figure 3.2 and Figure 3.3 affect directly the droplet vaporization rate to various certain extents. Generally speaking, higher latent heat and density tend to slow down the droplet vaporization rate; higher vapor pressure and specific heat will lead to a faster vaporization rate. Therefore, the vaporization rates of heptane, dodecane, tetradecane and hex-

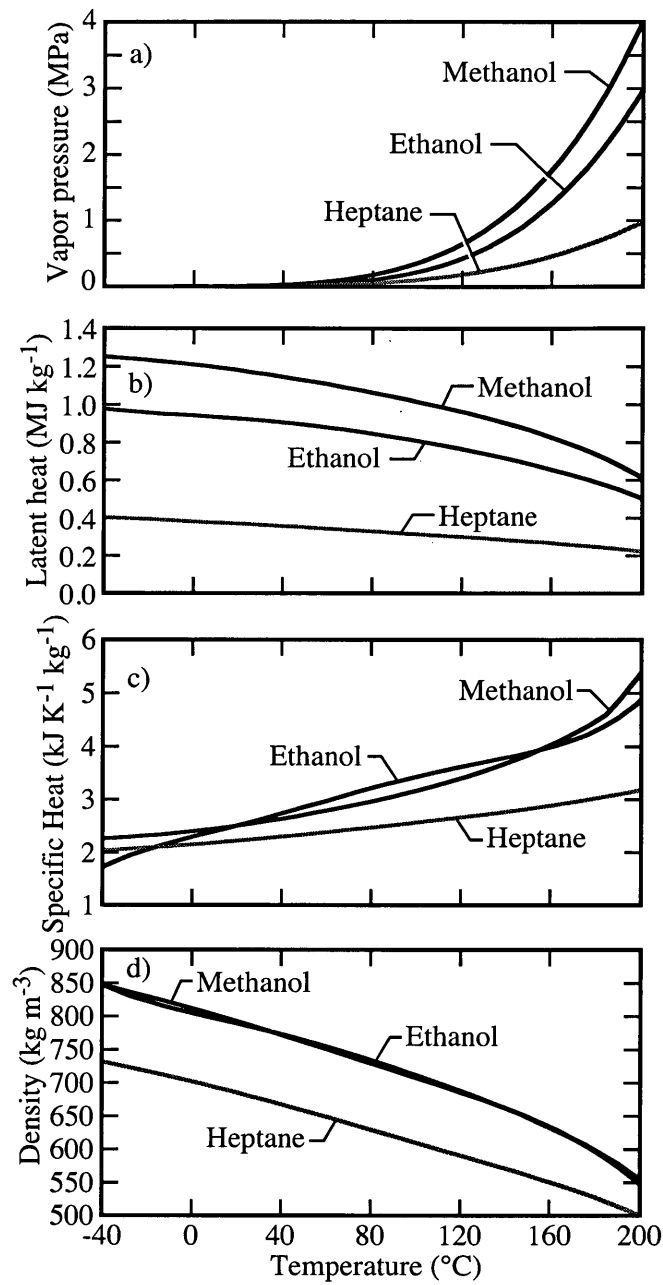


Figure 3.3: Physical properties of liquid heptane, methanol and ethanol.

adecane are in the decrease order under the same circumstance. Alcohols have slow vaporization rate than heptane because their high latent heat, heat capacity, and density.

CHAPTER 4

RESULTS AND DISCUSSION

The present studies use the mathematical models to investigate the vaporization performance of multicomponent liquid fuels, considering interactions of the strained flow field with the vaporizing droplets over a wide range of inlet parameters and operating conditions. As illustrated in Figure 4.1, the separation distance between inlet manifolds of the opposed-stagnation flow is set to be $L = 2$ cm. The gas compositions of both inlets are considered to be air. Three gas temperatures: 47, 500, and 700 °C, and two gas-phase pressure: 1 and 10 atm, are considered. Table 4.1 lists the liquid fuel compositions of the droplet at the inlet. Three liquid fuel mixtures are considered: 1). ethanol-heptane; 2). heptane-dodecane-tetradecane; 3). dodecane-tetradecane-hexadecane, with equal mole percentage for each liquid fuel component. Four droplet diameters: 10, 20, 30 and 50 μm are considered. Six global characteristic parameters are used to compare the vaporization performance of the multicomponent liquid fuels: droplet life time, droplet temperature, droplet component mole fractions, local gas-phase equivalence ratio, gas-phase temperature, and gas-phase component mole fractions. By varying the operating conditions, the droplet loading is adjusted such that the inlet fuel/air equivalence ratio ϕ is always set to be one.

4.1 Initial Equivalence Ratio and Droplet Loading

The initial droplet loading (i.e., at the left-hand boundary, Figure 1.1) is adjusted such that the inlet flow achieves a specified fuel/air equivalence ratio ϕ . That is

$$\phi = \frac{J_{\text{fuel}}/J_{\text{O}_2}}{(J_{\text{fuel}}/J_{\text{O}_2})_{\text{stoich}}}, \quad (4.1)$$

where J is a molar flux. The oxygen flux is evaluated as $J_{\text{O}_2} = \rho u X_{\text{O}_2} / \bar{W}$, where ρ and u are the gas-phase mass density and axial velocity, respectively, and \bar{W} is mean molecular weight. X_{O_2} is the mole fraction of oxygen within the gas-phase mixtures,

Table 4.1: Droplet compositions at the inlet

	CH ₃ OH	C ₂ H ₅ OH	C ₇ H ₁₆	C ₁₂ H ₂₆	C ₁₄ H ₃₀	C ₁₆ H ₃₄
Et+C7		0.85	0.15			
C7+C12+C14			1/3	1/3	1/3	
C12+C14+C16				1/3	1/3	1/3

and is equal to 0.21 for air. For a specified equivalence ratio the fuel molar flux is

$$J_{\text{fuel}} = \phi J_{\text{O}_2} (J_{\text{fuel}}/J_{\text{O}_2})_{\text{stoich}} \quad (4.2)$$

The fuel mass flux is

$$\dot{m}''_{\text{fuel}} = J_{\text{fuel}} W_{\text{fuel}}, \quad (4.3)$$

where W_{fuel} is the molecular weight of the fuel. For a specified initial droplet diameter d_0 , individual droplet mass $m_{d_0} = \rho_{\text{fuel}} \pi d_0^3 / 6$, and droplet velocity u_{d_0} , the initial droplet number density is

$$n_{d_0} = \frac{\dot{m}''_{\text{fuel}}}{m_{d_0} u_{d_0}}. \quad (4.4)$$

4.2 Ethanol-heptane Liquid Fuels

Consider first the vaporization characteristics of the droplet with a binary liquid fuel mixture: 85% C₂H₅OH and 15% C₇H₁₆. Three droplet diameters are studied: 5, 10 and 40 μm . Air is injected at both injectors at the same velocity of 1.0 m/s and temperature of 47 °C. The environment pressure is set to be 1 atm. The initial droplet loading is set to achieve an equivalence ratio of $\phi = 1$.

Figure 4.1 illustrates spatial solution profiles for the droplet with an initial diameter of 5 μm . As shown in the top panel of Figure 4.1, the droplet diameter decreases very fast from 5 μm at the inlet to about 3.5 μm at the axial position of 0.5 cm, during which about two-third of the droplet mass is vaporized. It should also be noted that the droplet mass decreases much faster than the diameter (the droplet mass depends on droplet volume, and hence the diameter cubed). The bottom panel

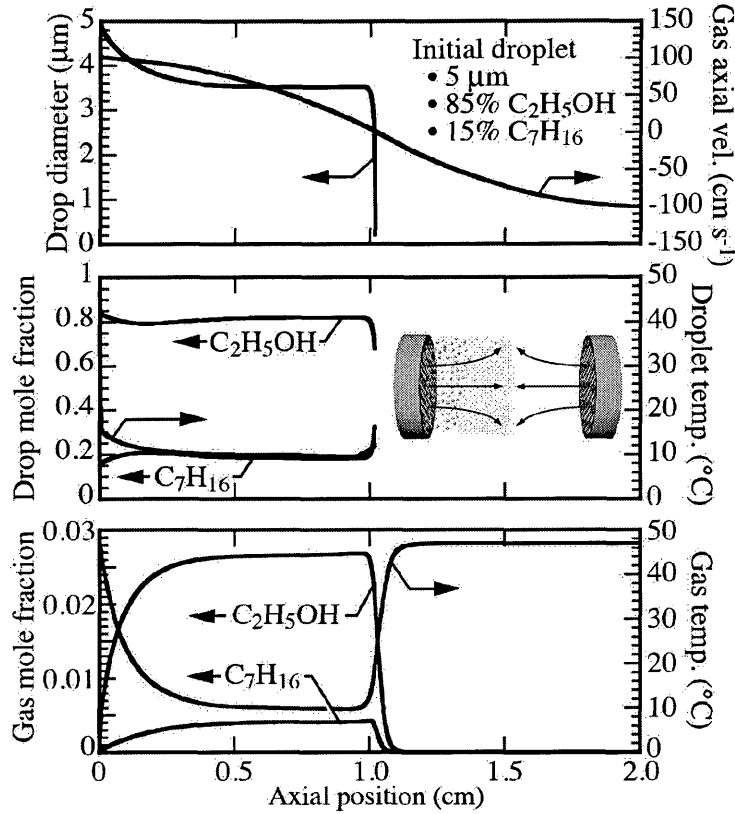


Figure 4.1: Solution profiles for $5 \mu\text{m}$ droplets with a composition of 85% $\text{C}_2\text{H}_5\text{OH}$ and 15% C_7H_{16} carried in air, $U_{\text{in}} = 100 \text{ cm s}^{-1}$, $T_{\text{in}} = 47 \text{ }^\circ\text{C}$, and $p = 1 \text{ atm}$.

of Figure 4.1 shows that the gas-phase compositions increase rapidly at this region, and the gas-phase temperature drops very fast from $47 \text{ }^\circ\text{C}$ to about $10 \text{ }^\circ\text{C}$. For the region of the axial position from 0.5 cm to 1.0 cm , Figure 4.1 shows that the variations of the droplet diameter, species compositions and temperatures are very small because the vaporization rate of the droplet is very low at the relatively low gas and droplet temperatures. At the stagnation position about 1.0 cm , the droplet meets the hot gas flowing from the opposite injector, the droplet vaporizes very fast as indicated in Figure 4.1 that the droplet diameter decreases on a nearly vertical asymptote near the stagnation plane. The middle panel of Figure 4.1 shows that the mole fraction of $\text{C}_2\text{H}_5\text{OH}$ decreases during the droplet vaporization processes while the mole fraction of C_7H_{16} increases, which indicates that $\text{C}_2\text{H}_5\text{OH}$ vaporizes faster than C_7H_{16} does.

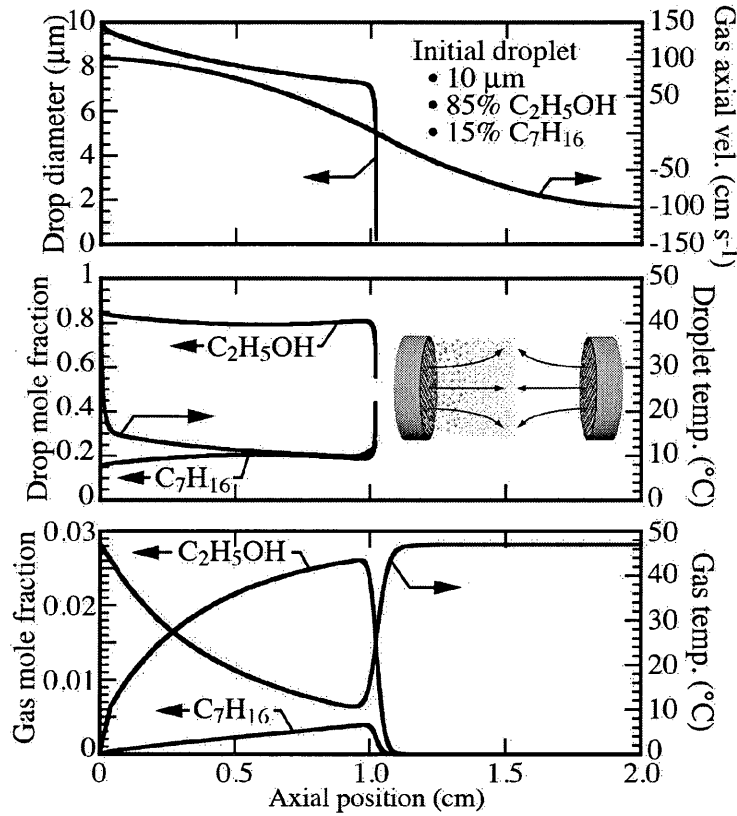


Figure 4.2: Solution profiles for $10 \mu\text{m}$ droplets with a composition of 85% $\text{C}_2\text{H}_5\text{OH}$ and 15% C_7H_{16} carried in air, $U_{\text{in}} = 100 \text{ cm s}^{-1}$, $T_{\text{in}} = 47 \text{ }^\circ\text{C}$, and $p = 1 \text{ atm}$.

Figure 4.2 and Figure 4.3 illustrate spatial solution profiles for the initial diameter of 10 and $40 \mu\text{m}$, respectively. Compared with Figure 4.1 for the initial diameter of $5 \mu\text{m}$, the smaller the initial droplet diameter is, the shorter the droplet lifetime is. An interesting point is that, as the droplet diameter increases, the droplet would go across the stagnation plane before completely vaporizing and even move back in reversing direction if the droplet is large enough. Because of the momentum associated with the droplets, the stagnation plane is at an axial position slightly greater than that of the centerline between the inlet burner surfaces. As the droplet diameter increases, the gas-phase mole fraction profiles show that the less liquid fuels are vaporized from the droplets. However, it does not mean that an individual larger droplet vaporizes slower compared with the small droplet. In fact, Equation 3.17 shows the droplet

vaporization rate is proportional to the droplet diameter. Since the initial equivalence ratio is set to be one, therefore, the total amount of droplet loading is fixed during the change of the droplet size. As the droplet diameter increases, the number density of the droplet becomes much smaller. If all the other conditions are the same, the total mass vaporization rate is inversely proportional to d^2 . Therefore, compared with the 5 μm -diameter droplet, the 40 μm -diameter droplet does vaporize much slower. Because of the slower vaporization rate at the larger droplet, the variation of the gas-phase temperature becomes smaller at the large droplet, and larger droplet generally lead to higher values of the minimum temperatures. The above figures also show that the minimum gas-phase and droplet temperatures are spatially located just upstream of the stagnation plane, where the relative cool gas and droplets are met by the onrushing relatively warm air. And most of the vaporization process for the large droplet takes place near the stagnation plane.

On the whole, Figure 4.1- Figure 4.3 also show that droplet diameter has little effects on the spatial gas-phase velocity profiles. But the gas-phase mole fractions and temperature can be affected largely by varying the inlet droplet diameter. Smaller droplets will lead to relatively low gas-phase temperature, but higher gas-phase fractions. And the large droplets could probably survive longer until the stagnation plane where most parts of the droplet vaporize completely. $\text{C}_2\text{H}_5\text{OH}$ vaporizes slightly faster than C_7H_{16} does.

4.3 Heptane-dodecane-tetradecane Liquid Fuels

Table 4.2 lists the operating parameters for a nominal case of the liquid fuel mixtures of C_7H_{16} , $\text{C}_{12}\text{H}_{26}$, and $\text{C}_{14}\text{H}_{30}$. At the inlet, the mole percentages for all the droplet fuel components are assumed to be the same (i.e., $X_{d,k} = 1/3$). The inlet gas-phase temperature is set to be 500 °C, and the inlet velocity is 200 cm/s. The inlet velocity of the droplet is also set to be 200 cm/s, but the droplet inlet temperature

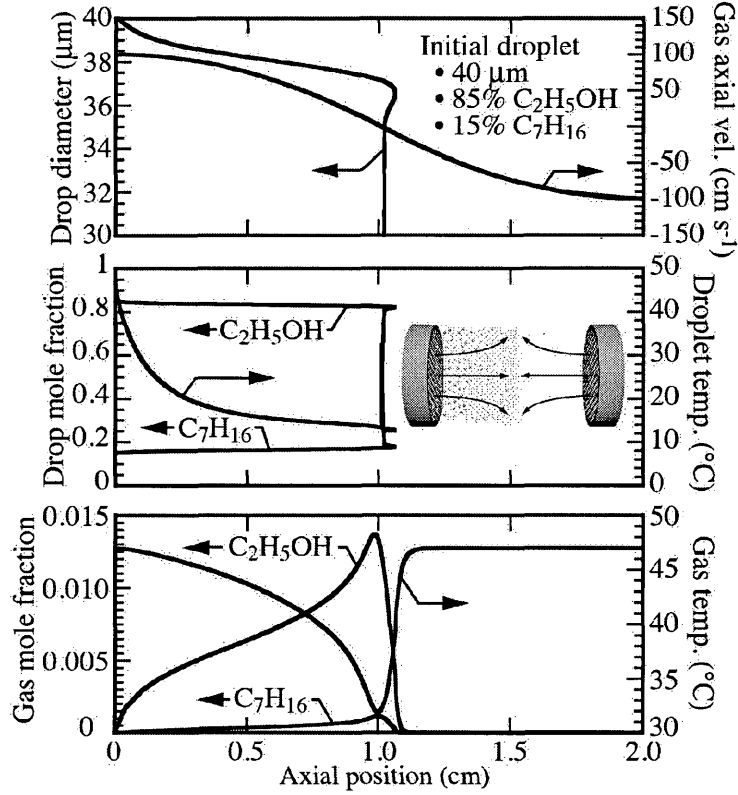


Figure 4.3: Solution profiles for 40 μm droplets with a composition of 85% $\text{C}_2\text{H}_5\text{OH}$ and 15% C_7H_{16} carried in air, $U_{\text{in}} = 100 \text{ cm s}^{-1}$, $T_{\text{in}} = 47 \text{ }^\circ\text{C}$, and $p = 1 \text{ atm}$.

Table 4.2: Baseline inlet parameters

	Droplet inlet	Opposed inlet
Gas composition	air	air
Gas temperature, T_0 ($^\circ\text{C}$)	500	500
Gas velocity, U_{in} (cm s^{-1})	200	200
Pressure, p (atm)	10	10
Droplet diameter, d_0 (μm)	50	
Droplet temperature, T_{d_0} ($^\circ\text{C}$)	47	
Droplet velocity (cm/s)	200	200
Equivalence ratio, ϕ	1	

is set to be 47 $^\circ\text{C}$. The droplet mass flow rate and number density is set such that the inlet equivalence ratio is 1. The gas-phase pressure is taken to be 10 atm. These operating conditions are used to simulate the vaporization processes within the diesel engine.

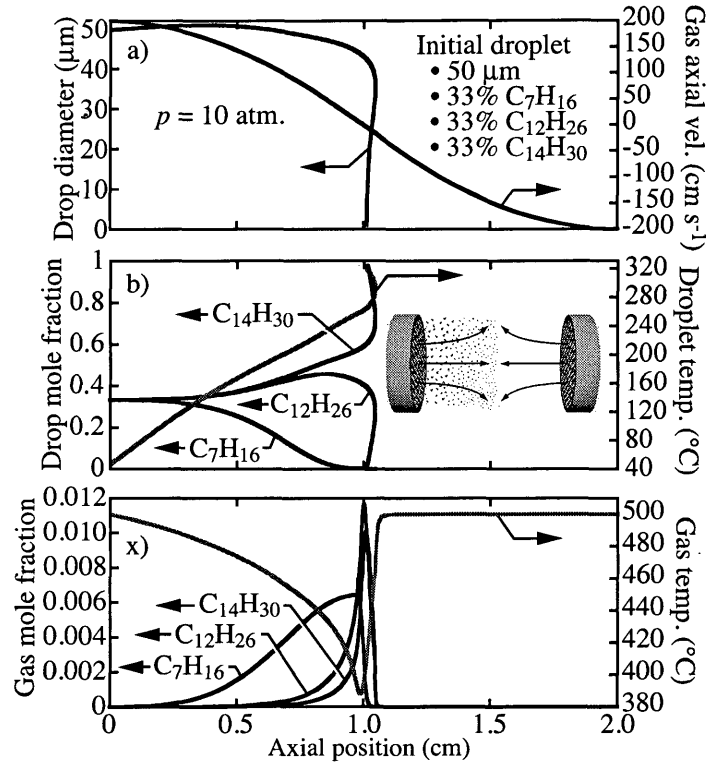


Figure 4.4: Solution profiles for 50 micron droplets with equal proportion of composition of heptane, dodecane, and tetradecane carried in air, $U_{\text{in}} = 200 \text{ cm s}^{-1}$, $T_{\text{in}} = 500 \text{ }^\circ\text{C}$, and $p = 10 \text{ atm}$.

Figure 4.4 illustrates the solution profiles. Since the inlet droplet temperature is much lower than the gas-phase temperature, the middle panel of Figure 4.4 shows that the droplet temperature increases steadily during the entire vaporization process. Because of the relatively large droplet size, the droplet can cross over the stagnation plane and also slightly move back before the droplet gets fully vaporized. The variation of the droplet composition is also illustrated in the middle panel of Figure 4.4. The gas-phase composition is illustrated in the bottom panel. At the region from the inlet to the axial position about 0.25 cm, the mole fractions of fuel species within the gas phase are very small, and the change of the liquid fuel mole fractions within the droplet is also very small, therefore, the vaporization rates for all the species are very small due to the relatively low droplet temperature. However, due to the increase of

the droplet temperature from the axial position of 0.25 cm to the stagnation plane, the mole fraction of the light species C_7H_{16} within the droplet decreases very fast to zero at the stagnation plane, the mole fractions of heavy species $C_{14}H_{30}$ increases steadily to one at the stagnation plane, and the $C_{12}H_{26}$ mole fraction increase along the axial position, but then decreases rapidly to zero near the stagnation plane. It shows that C_7H_{16} vaporize much faster from the droplet into the gas phase compared with the other two heavier species, and the vaporization rate of the heaviest species $C_{14}H_{30}$ is slowest, therefore only $C_{14}H_{30}$ is left within the droplet near the droplet lifetime. The comparison of the mole fractions profiles of the gas-phase species in the bottom panel also demonstrates the different vaporization rates.

Figure 4.5 compares the solution profiles by varying the inlet droplet diameter at the inlet gas-phase temperature of 500 °C. Four inlet droplet diameters are chosen: 10, 20, 30, and 50 μm . The left panels of Figure 4.5 compares the variations of the droplet diameter, droplet temperature, and also the droplet compositions during the droplet vaporization processes. The right panels shows the local gas-phase equivalence ratio, gas-phase temperature and also the gas-phase compositions. As the inlet droplet diameter decreases, Figure 4.5a shows that the droplets get fully vaporized earlier in the flow field due to the much faster droplet temperature increase (i.e. Figure 4.5b), which, in turn, results in much faster decrease of the gas-phase temperature (i.e. Figure 4.5g). Figure 4.5c,d,e illustrate the profiles of the droplet mole fractions. As the inlet droplet diameter becomes smaller, the spatial change of droplet compositions become stronger. However, the order of the vaporization rate for the liquid-fuel species are the same: $C_7H_{16} > C_{12}H_{26} > C_{14}H_{30}$. Because the smaller droplet is fully vaporized near the inlet, the profiles of the gas-phase mole fractions become flat after the axial position of the full vaporization (i.e., Figure 4.5h,i,j). Figure 4.5h,i,j also show that the flat mole fractions for all the species increase as the inlet droplet diameter increases, but the flat region becomes smaller. Particularly, at the inlet

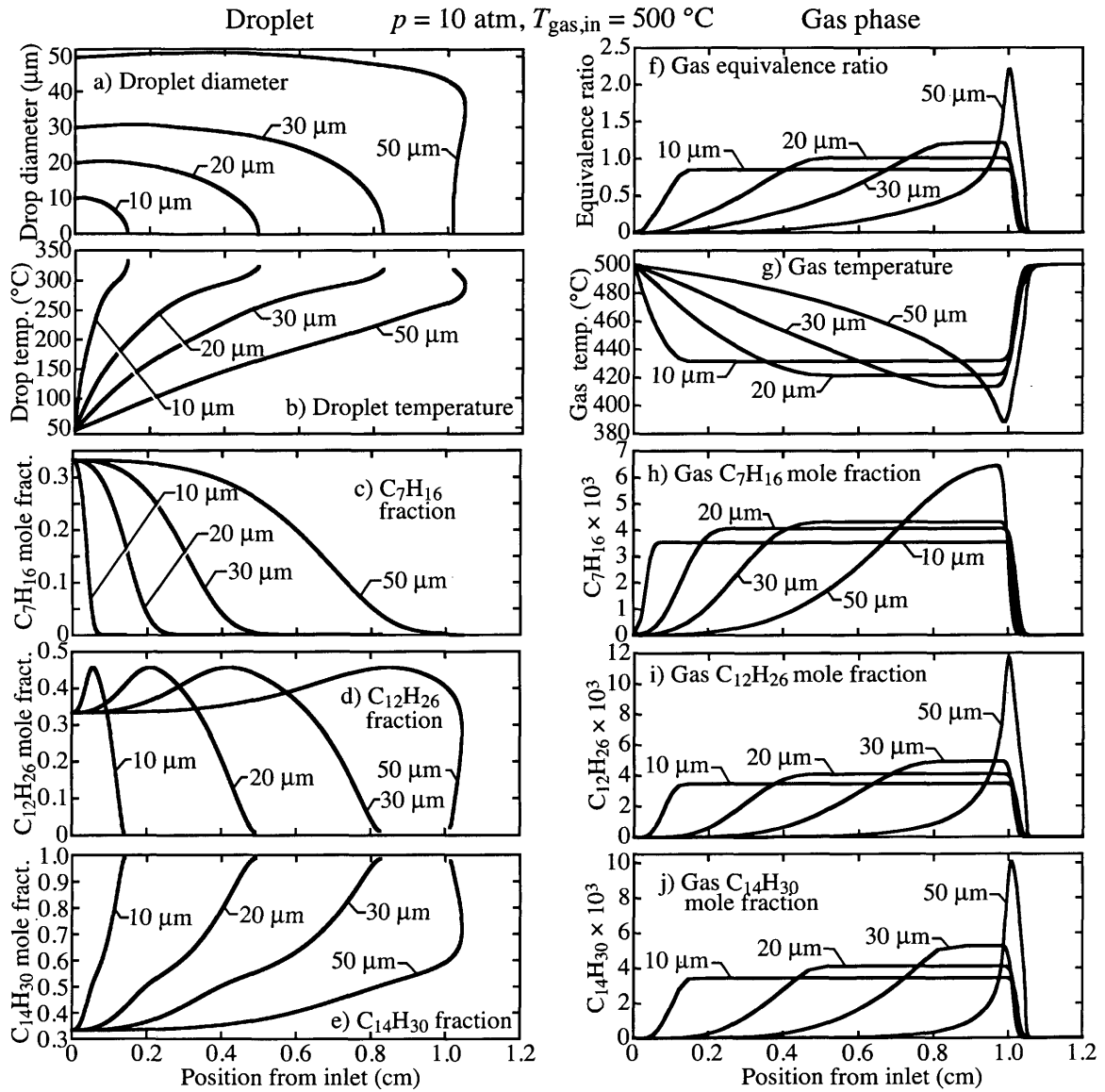


Figure 4.5: Comparison of the solution profiles for the inlet droplet diameters: 10, 20, 30, and 50 μm . The liquid fuel mixture at the inlet is C_7H_{16} , $\text{C}_{12}\text{H}_{26}$ and $\text{C}_{14}\text{H}_{30}$ with equal mole percentage. The inlet drop temperature $T_{d_0} = 47 \text{ }^\circ\text{C}$. The gas composition at both injectors is air with $U_{\text{in}} = 200 \text{ cm s}^{-1}$, $T_{\text{in}} = 500 \text{ }^\circ\text{C}$, and $p = 10 \text{ atm}$.

droplet diameter of 50 μm , there is almost no flat region any more, and the droplet is largely vaporized at the stagnation plane. It is also interesting to note that the maximum of the local equivalence ratio becomes bigger when increasing the inlet droplet diameter, and can even go beyond one at region of the the stagnation plane

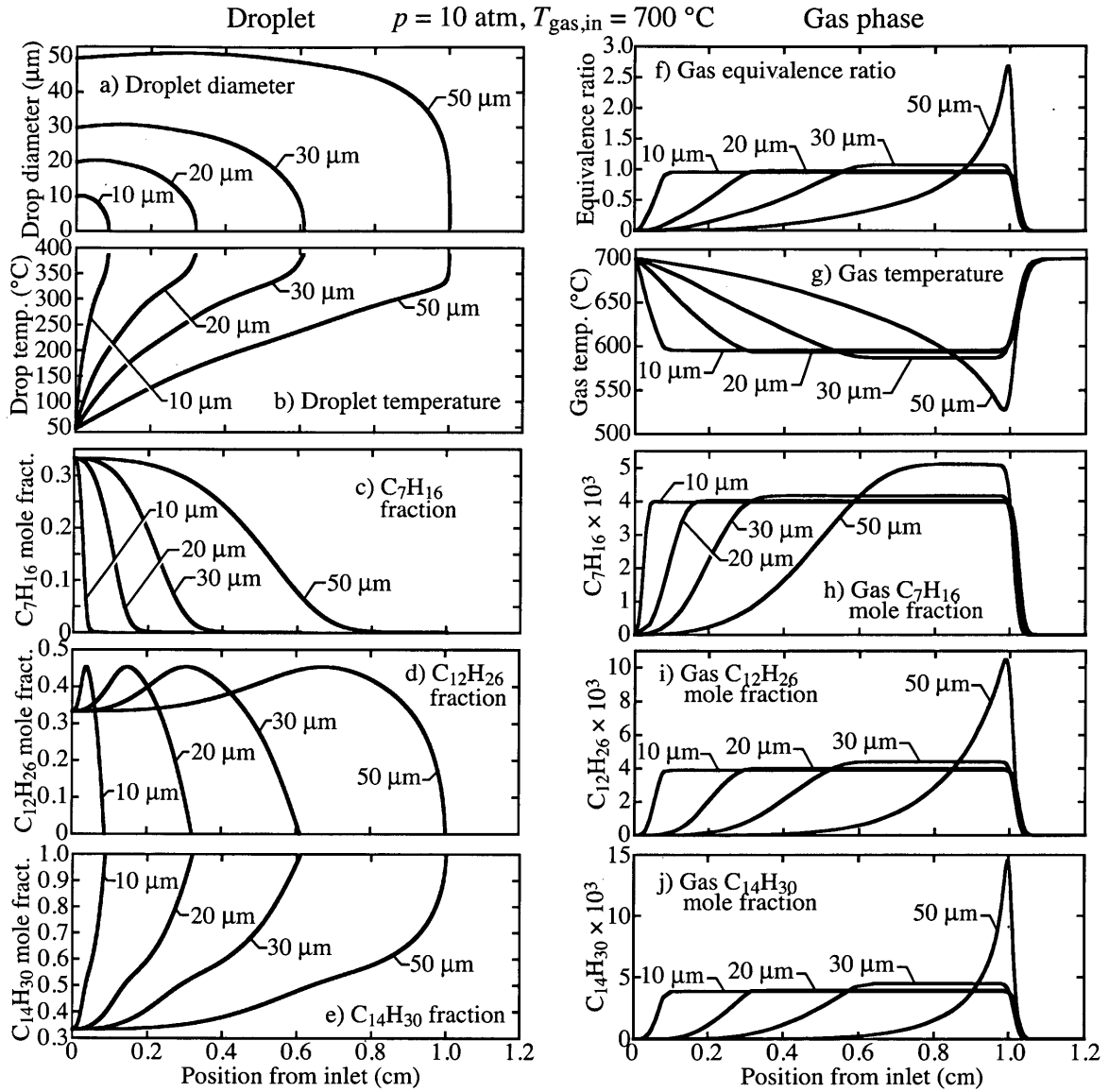


Figure 4.6: Comparison of the solution profiles for the inlet droplet diameters: 10, 20, 30, and 50 μm . The liquid fuel mixture at the inlet is C_7H_{16} , $\text{C}_{12}\text{H}_{26}$ and $\text{C}_{14}\text{H}_{30}$ with equal mole percentage. The inlet drop temperature $T_{d_0} = 47 \text{ }^\circ\text{C}$. The gas composition at both injectors is air with $U_{\text{in}} = 200 \text{ cm s}^{-1}$, $T_{\text{in}} = 700 \text{ }^\circ\text{C}$, and $p = 10 \text{ atm}$.

for the inlet droplet diameter of 50 μm .

Figure 4.6 compares the solution profiles under the same operating conditions as these in Figure 4.5 except that the inlet gas-phase temperature is increased to 700 $^\circ\text{C}$. Generally speaking, by increasing the inlet gas-phase temperature, the temperature

gradient between the gas phase and the droplet also increases, therefore, more heat is transferred into the droplet, resulting in higher droplet temperature. Because of the relatively hotter droplet, the droplet is vaporized more faster. Nevertheless, the general behaviors of the droplet vaporization are very similar.

4.4 Dodecane-tetradecane-hexadecane Liquid Fuels

Figure 4.7 compares the solution profiles using the liquid fuel mixture of $C_{12}H_{26}$, $C_{14}H_{30}$, and $C_{16}H_{34}$ with equal initial mole fractions at the initial droplet diameter of 10, 20, 30 and 50 μm . The inlet air temperature is 500 $^{\circ}\text{C}$ and the pressure is 10 atm. Here $C_{16}H_{34}$ is used to simulate the diesel fuel. Particularly the gas-phase thermodynamic data of $C_{16}H_{34}$ is used in this simulation while the liquid properties are based on the diesel fuel. Figure 4.8 illustrates the solution profiles for the inlet air temperature of 700 $^{\circ}\text{C}$.

Compared to Figure 4.5 and Figure 4.6 for the droplet fuel mixture of C_7H_{16} , $C_{12}H_{26}$ and $C_{14}H_{30}$, the overall vaporization behaviors illustrated in Figure 4.7 and Figure 4.8 are very similar: the lighter components vaporize faster, and heaviest component is the last one to get fully vaporized at the droplet lifetime. However, it takes longer time to vaporize the C12-C14-C16 droplet under the same operating conditions.

The investigations of influence factors on droplet vaporization indicate some vital points. It can be seen that decreasing droplet size, increasing gas-phase temperature, and making droplet components lighter have similar effects on droplet vaporization characteristics because all of these measures are to enhance droplet vaporization rate.

From the above parameter studies, general measures to enhance vaporization rates can be concluded. Atomize the droplet to smaller size, heating the liquid droplet fuel prior to injection, increasing the gas-phase temperature, decrease the operating pressure, and changing the droplet components to lighter components are general

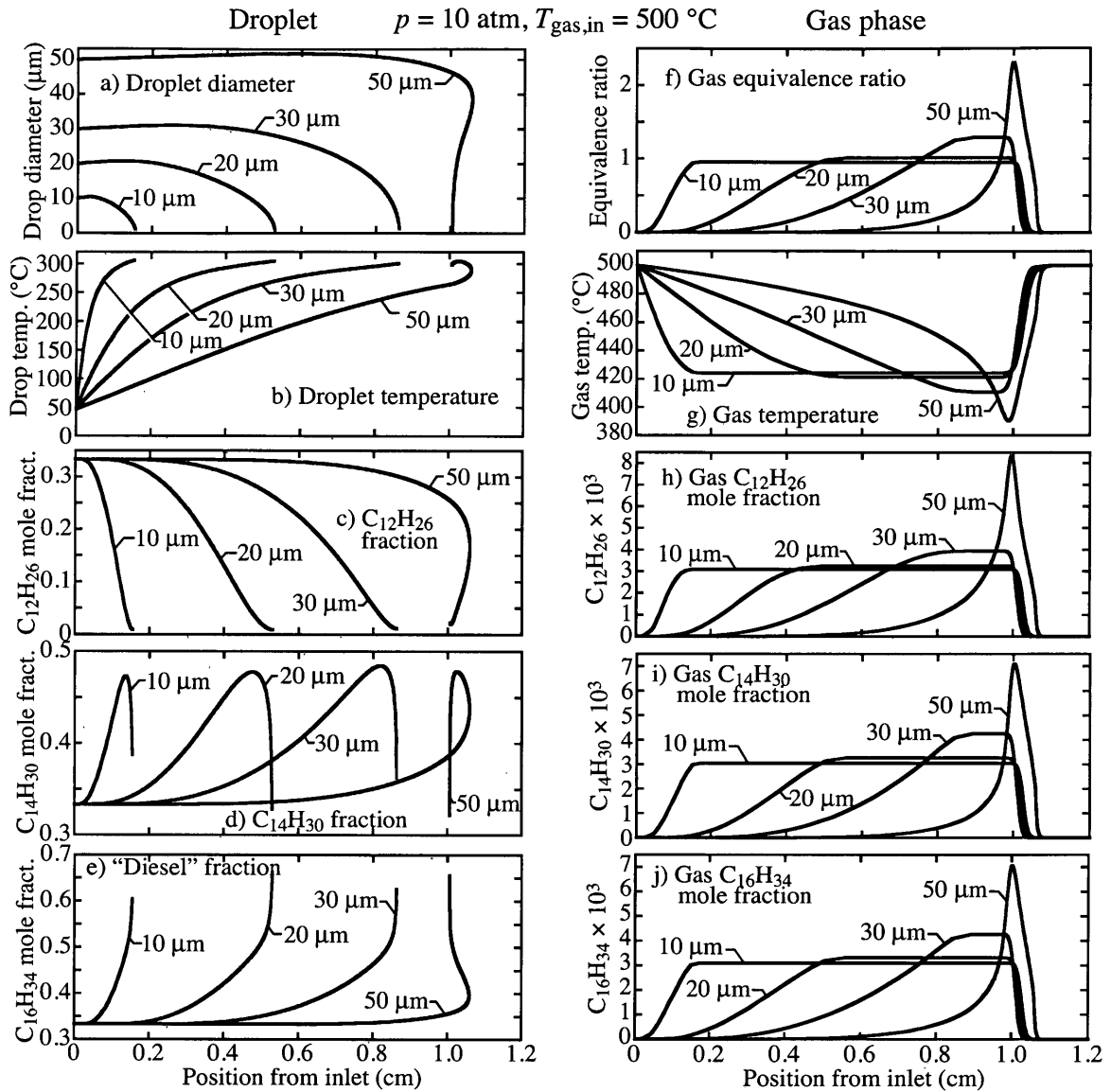


Figure 4.7: Comparison of the solution profiles for the inlet droplet diameters: 10, 20, 30, and 50 μm . The liquid fuel mixture at the inlet is $\text{C}_{12}\text{H}_{26}$, $\text{C}_{14}\text{H}_{30}$, and $\text{C}_{16}\text{H}_{34}$ with equal mole percentage. The inlet drop temperature $T_{d0} = 47 \text{ }^\circ\text{C}$. The gas composition at both injectors is air with $U_{\text{in}} = 200 \text{ cm s}^{-1}$, $T_{\text{in}} = 500 \text{ }^\circ\text{C}$, and $p = 10 \text{ atm}$.

effective ways to enhance droplet vaporization rate. Moreover, changing the relative velocity between droplet and gas phase also causes changes of vaporization rates, but it only has relatively small effects compared with measures listed above. In practical applications, combined methods could be adopted according to actual requirements.

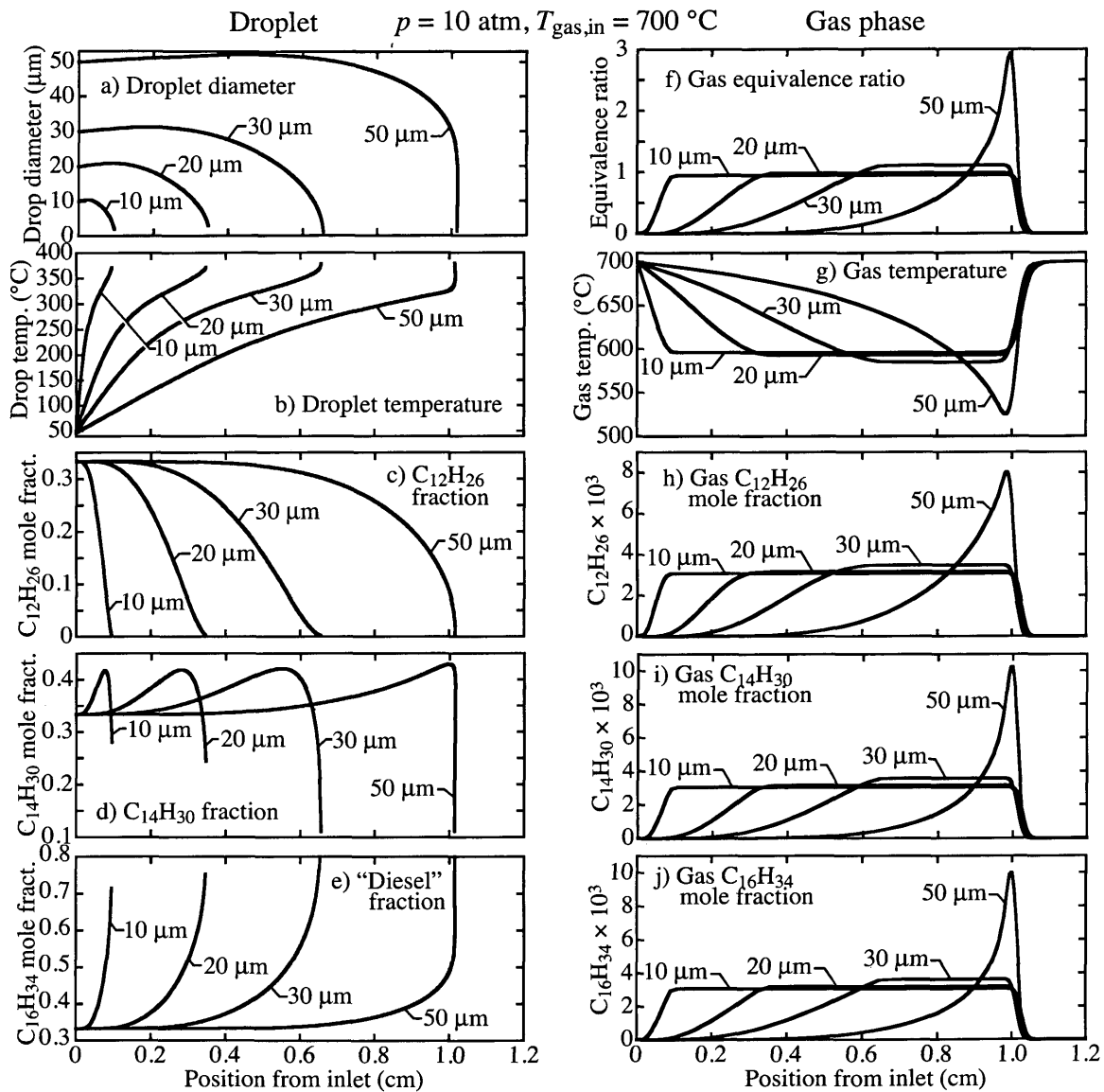


Figure 4.8: Comparison of the solution profiles for the inlet droplet diameters: 10, 20, 30, and 50 μm . The liquid fuel mixture at the inlet is $\text{C}_{12}\text{H}_{26}$, $\text{C}_{14}\text{H}_{30}$, and $\text{C}_{16}\text{H}_{34}$ with equal mole percentage. The inlet drop temperature $T_{d_0} = 47 \text{ }^\circ\text{C}$. The gas composition at both injectors is air with $U_{\text{in}} = 200 \text{ cm s}^{-1}$, $T_{\text{in}} = 700 \text{ }^\circ\text{C}$, and $p = 10 \text{ atm}$.

CHAPTER 5

SUMMARY AND CONCLUSIONS

Droplet vaporization plays a critical role in many combustion technologies, with liquid fuels usually being introduced as a multicomponent polydisperse spray into a turbulent flow field. The purpose of the present study is to assist understanding of these highly complex processes by developing and applying models of multicomponent droplet vaporization in an idealized, but representative, opposed stagnation-flow configuration. Because the configuration is far less complex than a practical combustor, it is possible to consider extensive parameter studies with personal-computer computational resources. The droplet's initial diameter, temperature, and composition are of particular interest in the present study. Operating conditions of particular interest include carrier-gas composition and temperature, inlet velocities (i.e., fluid mechanical strain rate), pressure, and droplet loading density. The quantitative insights derived from these fundamental studies can be used to assist practical combustor technology.

Liquid fuels are typically composed of multiple chemical components, each of which has its own thermochemical properties (i.e., density, vapor pressure, heat capacity, and latent heat of vaporization). These properties affect directly the droplet vaporization characteristics as well as the surrounding gas-phase flow field. This study considered four fuel mixtures: ethanol-heptane, heptane-dodecane-tetradecane, and dodecane-tetradecane-hexadecane.

The ethanol-heptane mixture is motivated by a need to understand how the performance of direct-injection-spark-ignition (DISI) engines may be affected by changes in fuel composition, especially alcohols. Currently, most DISI engines are designed for homogeneous-charge combustion, where the in-cylinder fuel injection, vaporization, and mixing is accomplished during the intake and early in the compression process. Thus the temperature and pressure are low, compared to post-compression conditions.

The heptane-dodecane-tetradecane and dodecane-tetradecane-hexadecane mixtures are motivated by diesel applications. In this case, the fuel is introduced near the end of the compression stroke where the temperature and pressure are relatively high.

The two-phase axisymmetric model is based upon an ideal opposed stagnation flow field. Liquid droplets are carried in one air stream that is met by an opposed air flow. Because of stagnation-flow similarity, the mathematical model can be represented as a one-dimensional boundary-value problem. Results show significant differences between different fuel mixtures, which have potentially important impacts on the design and modification of fuel-injection systems.

Some general observations can be drawn from the studies, many of which can be anticipated. Larger droplets vaporize more slowly than smaller droplets. Higher gas-phase temperatures cause faster vaporization than lower temperatures. More volatile components vaporize more readily than lower volatility components. The differential vaporization rates for multicomponent fuel blends affects the droplet composition during its lifetime, with the droplet becoming richer in the lower-volatility compounds late in its lifetime. Because the droplet composition changes during the droplet vaporization process, the surrounding gas-phase composition also changes. Thus, the local gas-phase fuel-air equivalence ratio varies. This variation, in turn, affects important combustion characteristics. Although many of the trends can be anticipated qualitatively, the models provide systematic and quantitative results. The results provided in this study could aid in further combustion research.

The present model provides significant new results and insights. Vaporization characteristics of common hydrocarbons are investigated, which can aid in the combustion research of these fuels. Nevertheless, some major enhancements can be envisaged in future research. The present model assumes that the composition is spatially uniform within the droplet. Depending on droplet size and liquid-phase diffusion coefficients, there could be compositional gradients within droplets. In this case, the

model could be extended by solving multicomponent diffusion equations within the vaporizing droplets.

The present model considers a monodispersed array of droplets. However, practical sprays are composed of polydispersed arrays of droplet sizes. Using approaches such as sectional methods, the model can be extended to consider polydispersion, but still retain stagnation-flow similarity.

The present model considers the thermodynamics of the gas phase and the vapor-pressure relationships to be ideal. For pressure up to around 10 atm, this assumption is reasonable. However, in a diesel engine after combustion is initiated, much higher pressures are encountered. In this case, non-ideal equations of state and thermodynamic relationship are needed.

The present model considers droplet vaporization, but does not incorporate the subsequent combustion. The model can be extended to include the coupled effects of gas-phase combustion kinetics and droplet vaporization. Such models have been previously developed for monodispersed droplets, where detailed chemistry and flame structure is considered. Beyond extending polydispersed droplets, the model should also be extended to include increasingly large and complex chemical kinetics mechanisms for higher hydrocarbons and practical logistics fuels (including aromatics). Although there are no principle problems to incorporating practical fuel chemistry, there are some important challenges to be overcome. On one hand, the large detailed reaction mechanisms for practical fuels must be developed and available. Because the reactions mechanisms can become very large (i.e., hundreds of species and thousands of reactions), the computational algorithms in the present models may need to be changed. For example, the direct solution of linear systems within the outer Newton iteration may need to be replaced by an iterative solution (e.g., preconditioned conjugate gradient) of the linear systems.

REFERENCES CITED

- [1] Abramzon, B., & Sirignano, W. A. 1989. Droplet vaporization model for spray combustion calculations. *Int. J. Heat Mass Transfer*, **32**, 1605–1618.
- [2] Allen, D.M., & Raabe, G.O. 1982. Re-evaluation of Millikan’s oil drop data for the motion of small particles in air. *J. Aerosol Sci.*, **6**, 537–547.
- [3] Barlow, R.S., Karpetis, A.N., Frank, J.H., & Chen, J.Y. 2001. Scalar profiles and NO formation in laminar opposed-flow partially premixed methane/air flames. *Combust. Flame*, **127**, 2102–2118.
- [4] Batchelor, K.G., & Shen, C. 1985. Thermophoretic deposition of particles in gas flowing over cold surfaces. *J. Colloid Interface Sci.*, **107**, 21–37.
- [5] Bellan, J., & Cuffel, R. 1983. A theory of nondilute spray evaporation based upon multiple drop interactions. *Combust. Flame*, **51**, 55–67.
- [6] Bellan, J., & Harstad, K. 1987a. Analysis of the convective evaporation of nondilute clusters of drops. *Int. J. Heat Mass Transfer*, **30**, 125–136.
- [7] Bellan, J., & Harstad, K. 1987b. The details of the convective evaporation of dense and dilute clusters of drops. *Int. J. Heat Mass Transfer*, **30**, 1083–1093.
- [8] Burger, M., Schmehl, R., Prommersberger, P., Schaefer, O., Koch, R., & Wittig, S. 2002. A multi-component droplet evaporation model for real aviation fuels at elevated pressures. *ILASS-Europe*.
- [9] Catoire, F., Gauthier, J.E.D., Bardon, M. F., & Benaissa, A. 1999. Quasi-steady evaporation for real multi-component fuel droplets. *J. I. Energy*, **72**, 134–142.
- [10] Chen, G., & Gomez, A. 1992. Counterflow Diffusion Flames of Quasi-monodisperse Electrostatic Sprays. *Proc. Combust. Inst.*, **24**, 1531–1539.
- [11] Continillo, G., & Sirignano, W.A. 1990. Counterflow spray combustion modeling. *Combust. Flame*, **81**, 325–340.
- [12] Davis, E. J., Ravindran, P., & Ray, A. K. 1981. Single aerosol particle studies. *Adv. Colloid Interface Sci.*, **15**, 1–24.
- [13] Deuffhard, P., Hairer, E., & Zugck, J. 1987. One-step and extrapolation methods for differential-algebraic systems. *Num. Math.*, **51**, 501–516.

- [14] Dillon, H.E., & Penoncello, S.G. 2004. A Fundamental Equation for the Calculation of the Thermodynamic Properties of Ethanol. *Int. J. Thermophysics*, **25**, 321–335.
- [15] E, P. Ravindran, & Davis, J. 1982. Multicomponent evaporation of single aerosol droplets. *J. Colloid Interface Sci*, **85**, 278–288.
- [16] E.W. Lemmon, M.O. McLinden, & Friend, D.G. 2010. *Thermophysical Properties of Fluid Systems*. Gaithersburg MD: National Institute of Standards and Technology. <http://webbook.nist.gov>.
- [17] Godsave, G. A. E. 1953. Studies of the combustion of drops in a fuel spray—the burning of single drops of fuel. *Fourth Symp. Int. Combust.*, pp, 818–830.
- [18] Grcar, J.F., Kee, R.J., Smooke, M.D., & Miller, J.A. 1986. A Hybrid Newton/Time-Integration Procedure for the Solution of Steady, Laminar, One-Dimensional Premixed Flames. *Proc. Combust. Inst.*, **21**, 1773–1782.
- [19] Gutheil, E., & Sirignano, W.A. 1998. Counterflow Spray Combustion Modeling with Detailed Transport and Detailed Chemistry. *Combust. Flame*, **113**, 92–105.
- [20] Hallett, W L.H. 2000. A simple Model for the vaporization of droplet with large numbers of components. *Combust. Flame*, **121**, 334–344.
- [21] Kee, R J., Yamashita, K., Zhu, H., & Dean, A M. 2011. The effects of liquid-fuel thermophysical properties, carrier-gas composition, and pressure, on strained opposed-flow non-premixed flames. *Combust. Flame*, **158**, 1129–1139.
- [22] Kee, R.J., Dixon-Lewis, G., Warnatz, J., Coltrin, M.E., & Miller, J.A. 1986. *A Fortran Computer Code Package for the Evaluation of Gas-Phase Multicomponent Transport Properties*. Tech. rept. SAND86-8246. Sandia National Laboratories.
- [23] Kee, R.J., Rupley, F.M., & Miller, J.A. 1987. *The CHEMKIN thermodynamic database*. Tech. rept. SAND87-8215. Sandia National Laboratories.
- [24] Kee, R.J., Rupley, F.M., Meeks, E., & Miller, J.A. 1996. *CHEMKIN-III: A Fortran Chemical Kinetics Package for the Analysis of Gas-phase Chemical and Plasma Kinetics*. Tech. rept. SAND96-8216. Sandia National Laboratories.
- [25] Kee, R.J., Coltrin, M.E., & Glarborg, P. 2003. *Chemically Reacting Flow: Theory and Practice*. Hoboken, NJ: John Wiley.
- [26] Law, C. K. 1982. Recent advances in droplet vaporization and combustion. *Prog. Energy Combust. Sci.*, **8**, 171–201.

- [27] Law, C. K., Prakash, S., & Sirignano, W. A. 1977. Theory of convective transient, multicomponent droplet vaporization. *Symp. Int. Combust.*, **16**, 605–617.
- [28] Lentati, A.M, & Chelliah, H.K. 1998. Dynamics of water droplets in a counterflow field and their effect on flame extinction. *Combust. Flame*, **115**, 158–179.
- [29] Li, S.C. 1997. Spray stagnation flames. *Prog. Energy Combust. Sci.*, **23**, 303–347.
- [30] Lutz, A.E., Kee, R.J., Grcar, J.F., & Rupley, F. M. 1997. *OPPDIF: A Fortran Program for Computing Opposed-Flow Diffusion Flames*. Tech. rept. SAND96-8243. Sandia National Laboratories.
- [31] Modak, A.U., Abbud-Madrid, A., Delplanque, J., & Kee, R.J. 2006. The effect of mono-dispersed water mist on the suppression of laminar premixed hydrogen-, methane-, and propane-air flames. *Combust. Flame*, **144**, 103–111.
- [32] Nishiwaki, N. 1955. Kinetics of liquid combustion processes: Evaporation and ignition lag of fuel droplets. *Fifth Symp. Int. Combust.*, pp, 148–158.
- [33] Prommersberger, K., Maier, G., & Wittig, S. 1998. Validation and application of a droplet evaporation model for real aviation fuel. *RTO AVT Symp. on "Gas Turbine Engine Combustion, Emissions and Alternative Fuels"*.
- [34] Ra, Y., & Reitz, R. 2009. A vaporization model for discrete multi-component fuel sprays. *Int. J. Multiphase Flow*, **35**, 101–117.
- [35] Rivard, E., & Bruggemann, D. 2010. Numerical investigation of semi-continuous mixture droplet vaporization at low temperature. *Chem. Eng. Sci.*, **65**, 5137–5145.
- [36] Rubaneja, P. L., & Sirignano, W. A. 1981. Theory of transient, multicomponent droplet vaporization in a convective field. *Eighteenth Sympo. Int. Combust.*, **18**, 1365–1374.
- [37] Sazhin, S.S., Kristyadi, T., Abdelghaffar, W.A., & Heikal, M.R. 2006. Models for fuel droplet heating and evaporation: Comparative analysis. *Fuel*, **85**, 1613–1630.
- [38] Sazhin, S.S., Elwardany, A., Krutitskii, P.A., Castanet, G., Lemoine, F., Sazhina, E.M., & Heikal, M.R. 2010. A simple model for bi-component droplet heating and evaporation. *Heat Mass Transfer*, **53**, 4495–4505.
- [39] Sirignano, W. A. 1983. Fuel droplet vaporization and spray combustion theory. *Prog. Energy Combust. Sci.*, **9**, 291–322.

- [40] Sirignano, W.A. 2010. *Fluid Dynamics and Transport of Droplets and Sprays*. Second edn. Cambridge University Press.
- [41] S.Sazhin. 2006. Advanced models of fuel droplet heating and evaporation. *Prog. Energy Combust. Sci*, **32**, 162–214.
- [42] Stefan, J., & Wiener, B. 1889. On evaporation and solutions as process of diffusion. *Intelligence and Miscellaneous Articles*, 139–140.
- [43] Talbot, L., Cheng, K.R., Schefer, W.R., & Willis, R.D. 1980. Thermophoresis of particles in a heated boundary layer. *J. Fluid Mech.*, **101**, 737–758.
- [44] Tamim, J., & Hallett, W. L. H. 1995. A continuous thermodynamics model for multi-component droplet vaporization. *Chem. Eng. Sci*, **50**, 2933–2942.
- [45] Turns, S. R. 1996. *An introduction to combustion-Concepts and applications*. McGraw-Hill, New York.
- [46] Watanabe, H., Matsushita, Y., Aoki, H., & Miura, T. 2010. Numerical simulation of emulsified fuel spray combustion with puffing and micro-explosion. *Combust. Flame*, **157**, 839–852.
- [47] Williams, F. A. 1959. Spray combustion theory. *Combust. Flame*, **3**, 215–228.
- [48] Williams, F. A. 1961. Progress in spray-combustion analysis. *Symp. Int. Combust.*, **8**, 50–69.
- [49] Williams, F. A. 1965. On vaporization of mist by radiation. *Int. J. Heat Mass Transfer*, **8**, 575–587.
- [50] Wood, B. J., Wise, H., & Inami, S. H. 1960. Heterogeneous combustion of multicomponent fuels. *Combust. Flame*, **4**, 235–242.
- [51] Yang, W., & Kee, R.J. 2002. The Effect of Monodispersed Water Mists on the Structure, Burning Velocity, and Extinction Behavior of Freely Propagating, Stoichiometric, Premixed, Methane-Air Flames. *Combust. Flame*, **130**, 322–335.
- [52] Zhang, L., & Kong, S. 2009. Modeling of multi-component fuel vaporization and combustion for gasoline and diesel spray. *Chem. Eng. Sci*, **64**, 3688–3696.
- [53] Zhang, L., & Kong, S. 2010. Vaporization modeling of petroleum-biofuel drops using a hybrid multi-component approach. *Combust. Flame*, **157**, 2165–2174.